Available online at www.sciencedirect.com
ScienceDirect
Journal of Computational Physics 227 (2008) 8209–8253
JOURNAL OF COMPUTATIONAL PHYSICS
www.elsevier.com/locate/jcp

A unified framework for the construction of one-step finite volume and discontinuous Galerkin schemes on unstructured meshes

Michael Dumbser [a,c,*], Dinshaw S. Balsara [b], Eleuterio F. Toro [a], Claus-Dieter Munz [c]

[a] Laboratory of Applied Mathematics, University of Trento, Via Mesiano 77, I-38100 Trento, Italy
[b] Physics Department, University of Notre Dame du Lac, 225 Nieuwland Science Hall, Notre Dame, IN 46556, USA
[c] Institut für Aerodynamik und Gasdynamik, Pfaffenwaldring 21, D-70550 Stuttgart, Germany

Received 12 December 2007; received in revised form 9 May 2008; accepted 13 May 2008
Available online 10 June 2008

Abstract

In this article, a conservative least-squares polynomial reconstruction operator is applied to the discontinuous Galerkin method. In a first instance, piecewise polynomials of degree N are used as test functions as well as to represent the data in each element at the beginning of a time step. The time evolution of these data and the flux computation, however, are then done with a different set of piecewise polynomials of degree $M \geqslant N$, which are reconstructed from the underlying polynomials of degree N. This approach yields a general, unified framework that contains as two special cases classical high order finite volume (FV) schemes ($N = 0$) as well as the usual discontinuous Galerkin (DG) method ($N = M$). In the first case, the polynomial is reconstructed from cell averages, for the latter, the reconstruction reduces to the identity operator. A completely new class of numerical schemes is generated by choosing $N \neq 0$ and $M > N$. The reconstruction operator is implemented for arbitrary polynomial degrees N and M on unstructured triangular and tetrahedral meshes in two and three space dimensions.

To provide a high order accurate one-step time integration of the same formal order of accuracy as the spatial discretization operator, the (reconstructed) polynomial data of degree M are evolved in time locally inside each element using a new *local* continuous space–time Galerkin method. As a result of this approach, we obtain, as a high order accurate predictor, space–time polynomials for the vector of conserved variables and for the physical fluxes and source terms, which then can be used in a natural way to construct very efficient *fully-discrete* and *quadrature-free* one-step schemes. This feature is particularly important for DG schemes in three space dimensions, where the cost of numerical quadrature may become prohibitively expensive for very high orders of accuracy.

Numerical convergence studies of all members of the new general class of proposed schemes are shown up to sixth-order of accuracy in space *and time* on unstructured two- and three-dimensional meshes for two very prominent nonlinear hyperbolic systems, namely for the Euler equations of compressible gas dynamics and the equations of ideal magnetohydrodynamics (MHD). The results indicate that the new class of intermediate schemes ($N \neq 0, M > N$) is computationally more efficient than classical finite volume or DG schemes.

* Corresponding author. Address: Institut für Aerodynamik und Gasdynamik, Pfaffenwaldring 21, D-70550 Stuttgart, Germany. Tel.: +39 349 88 37 064; fax: +49 711 6856 3438.
E-mail addresses: michael.dumbser@ing.unitn.it (M. Dumbser), dbalsara@nd.edu (D.S. Balsara), toro@ing.unitn.it (E.F. Toro), munz@iag.uni-stuttgart.de (C.-D. Munz).

0021-9991/$ - see front matter
doi:10.1016/j.jcp.2008.05.025

Finally, a large set of interesting test cases is solved on unstructured meshes, where the proposed new time stepping approach is applied to the equations of ideal and relativistic MHD as well as to nonlinear elasticity, using a standard high order WENO finite volume discretization in space to cope with discontinuous solutions.

Keywords: Hyperbolic PDE; Unstructured meshes; Finite volume; Discontinuous Galerkin; *M*-exact $P_N P_M$ least squares reconstruction; One-step time discretization; Local continuous space–time Galerkin method; WENO; Euler equations; Ideal and relativistic MHD equations; Nonlinear elasticity

1. Introduction

The idea of applying a reconstruction operator to the DG method in order to enhance accuracy was first introduced by Cockburn et al. [16] and further developed by Ryan et al. [62]. However, they applied the reconstruction operator only at the final output time and therefore called their method a postprocessing technique for DG. Obviously, this kind of accuracy enhancement becomes problematic on reasonably *coarse* meshes in space and time for general nonlinear time dependent problems, where discretization errors (temporal *and* spatial errors) necessarily accumulate during time stepping and thus information that is once lost due to any kind of discretization error can never be completely recovered. Therefore, Dumbser and Munz [25,31] were the first to propose the application of a reconstruction operator to the DG scheme at the beginning of each time step. The advantages of the proposed tensor product reconstruction on Cartesian grids were: First, the formal order of accuracy of a DG scheme using basis functions of degree N was increased to $3N + 3$. Second, the resulting reconstructed DG scheme could be directly applied to the diffusion equation by simply using a central flux formulation, yielding a much larger stability limit than the classical local DG schemes [19,21]. Another possibility to combine the DG method with a reconstruction operator in order to discretize diffusion equations can also be found in the recent work by van Leer and Nomura [80]. Nonlinear versions of reconstruction operators are also applied to DG schemes in order to serve as limiters, as in the HWENO approach introduced by Qiu and Shu [59,60] and as also recently furthered by Balsara et al. [5].

In this article, we propose a linear, i.e. a non-data dependent, reconstruction operator for DG schemes on general unstructured triangular and tetrahedral meshes in two and three space dimensions, respectively. A nonlinear version of this reconstruction operator is already available in form of a WENO method in the pure finite volume context [28,29] and will be extended to the full general new class of methods in subsequent work since it would be out of the scope of this article to deal with nonlinear reconstruction operators for the general case.

The reconstruction is applied to polynomials of degree N, spanned by orthogonal basis functions Φ_l and generates piecewise polynomials of any degree $M \geqslant N$, spanned by hierarchical orthogonal basis functions Ψ_l. The basis functions Ψ_l are chosen such that up to degree N they coincide with the basis functions Φ_l and that the functions Ψ_l with degree larger than N are *orthogonal* to all Φ_l. Furthermore, general conservation of all degrees of freedom up to degree N is imposed. These particular properties of the proposed reconstruction operator will be of significant importance for the resulting numerical scheme. In the following, we use the notation $P_N P_M$ for reconstructed DG schemes using Nth degree test functions and original basis functions and Mth degree reconstruction polynomials that are used for time integration and flux evaluation. It is obvious that in this proposed general framework of using a reconstruction operator together with DG schemes, the special case of choosing $N = 0$ yields classical (high order) finite volume schemes and that the choice $N = M$ is equivalent to the classical discontinuous Galerkin method. In the latter case, the reconstruction reduces to the identity operator. For $N \neq 0, N > M$ we obtain a new class of numerical methods from third-order of accuracy upwards, that could be either denoted as Hermite finite volume schemes or reconstructed discontinuous Galerkin methods. For a graphical illustration of the different methods and their relationships, see Fig. 1. Note that nonlinear HWENO versions of the $P_1 P_2$ and $P_1 P_3$ schemes have already been developed for structured meshes by Balsara et al. [5].

For the construction of a high order one-step time discretization that is automatically of the same order of accuracy as the space discretization, we propose a new approach that evolves the (reconstructed) polynomials

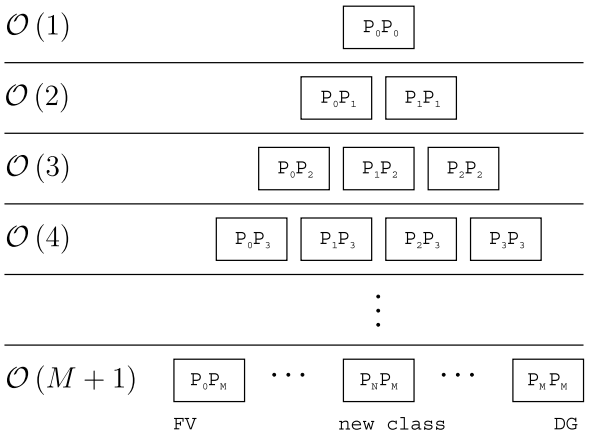

Fig. 1. Classification of the proposed P_NP_M schemes. The leftmost branch ($N = 0$) coincides with standard finite volume schemes and the rightmost branch ($N = M$) with classical DG schemes. From third-order on, there is a new class of intermediate schemes in between those branches.

of degree M locally inside each element using a *local* weak formulation of the governing PDE in space–time, which is approximated by a *local continuous* space–time Galerkin method. This approach is more general than those based on an analytic or semi-analytic version of the Cauchy–Kovalewski or Lax–Wendroff procedure, such as the original ENO scheme of Harten et al. [44], the ADER approach of Toro et al. [73,70,74,64,71,72,49,32,68,28,29] and other Cauchy–Kovalewski procedure based methods [34,58,57,53,37]. The continuous local space–time Galerkin method used in this article has lower computational complexity and is substantially easier to implement than the *local discontinuous* space–time Galerkin method introduced recently by Dumbser et al. for hyperbolic balance laws with stiff source terms [26]. Within the proposed continuous space–time Galerkin approach a full set of space–time polynomials is produced for the conservative variables as well as for the physical fluxes of the governing PDE. This allows the construction of quadrature-free, see [2], one-step schemes for nonlinear PDE that only solve one Riemann problem per element interface, independent of the order of accuracy of the scheme. Using the evidence of a numerical von-Neumann stability analysis we will show that the stability of the resulting reconstructed P_NP_M DG schemes depends only on the degree N of the test functions and not on the degree M of the reconstructed polynomials. This means, in contrast to usual DG schemes, that the explicit time step limit is not restricted by the final order of the method (except for the case $N = M$), but by the degree of the underlying data representation.

The three key points of the proposed schemes, which also serve as guiding themes for this article, are: first of all, the construction of the new general reconstruction operator for P_NP_M DG schemes on unstructured triangular and tetrahedral meshes (Section 2). Second, the new time discretization method (Section 3). Third, using the previous two ingredients, the construction of efficient quadrature-free and fully-discrete one-step schemes (Section 4). A detailed analysis of the linear stability as well as the accuracy and efficiency of the proposed schemes are shown in Section 5. In Section 6 we underscore the generality of the proposed new time discretization compared to previous Cauchy–Kovalewski procedure based one-step methods and will apply the nonlinear WENO finite volume version ($N = 0$) of our schemes to three complicated and challenging hyperbolic systems, namely the ideal and relativistic MHD equations and the equations of nonlinear elasticity. In Section 7 we give a conclusion with outlook towards future work.

2. The P_NP_M reconstruction operator on unstructured meshes

The main ingredient of the proposed P_NP_M discontinuous Galerkin schemes is a direct extension of the reconstruction algorithm proposed in [28,29] for finite volume schemes. The computational domain Ω is discretized by conforming elements $T^{(m)}$, indexed by a unique mono-index m ranging from 1 to the total number of elements E. The elements are chosen to be triangles in 2D and tetrahedrons in 3D. The union of all elements is called the triangulation or tetrahedrization of the domain, respectively,

$$\mathcal{T}_\Omega = \bigcup_{m=1}^{E} T^{(m)}. \tag{1}$$

As usual also for standard DG schemes, the numerical solution u_p of the vector of conserved quantities is represented at the beginning of a time-step by piecewise polynomials of degree N inside an element as a sum of degrees of freedom $\hat{u}_p^{(m)}$ and the space-only dependent basis functions of degree N as follows:

$$u_p^{(m)}(\vec{\xi}, t^n) = \hat{u}_{pl}^{(m)}(t^n)\Phi_l(\vec{\xi}), \tag{2}$$

where $\vec{\xi} = (\xi, \eta, \zeta)^{\mathrm{T}}$ are the spatial coordinates in a reference coordinate system, see Fig. 2, where also the reference elements T_E are defined. The equations for the transformation can be found in [28,29]. As short notation for the mapping and its inverse mapping from $\vec{\xi} = (\xi, \eta, \zeta)$ to $\vec{x} = (x, y, z)$ and vice versa with respect to the element $T^{(m)}$, we simply write

$$\vec{x} = \vec{x}(T^{(m)}, \vec{\xi}), \qquad \vec{\xi} = \vec{\xi}(T^{(m)}, \vec{x}). \tag{3}$$

Via the inverse mapping given in (3) for the vector $\vec{\xi}$, the element $T^{(m)}$ is transformed to the unit element T_E, whose volume is $|T_E| = \frac{1}{2}$ in two dimensions and $|T_E| = \frac{1}{6}$ in three space dimensions, respectively. Furthermore,

$$J_{ij} = \frac{\partial x_i}{\partial \xi_j} \tag{4}$$

is the Jacobian matrix of the transformation and $|J| = |J_{ij}|$ its determinant, being equal to twice the triangle's surface in 2D and equal to six times the tetrahedron's volume in 3D. Throughout the paper we use classical tensor notation, which implies summation over each index appearing twice.

In our proposed approach, we now apply a reconstruction operator on these data in order to achieve an even higher order of accuracy for the spatial discretization. At time t^n the reconstructed numerical solution w_p of the conserved variables is written for element $T^{(m)}$ as

$$w_p^{(m)}(\vec{\xi}, t^n) = \hat{w}_{pl}^{(m)}(t^n)\Psi_l(\vec{\xi}), \tag{5}$$

where the reconstruction basis functions Ψ_l are polynomials of degree $M \geqslant N$. The index l ranges from 1 to its maximum value L_N in Eq. (2), and to L_M in Eq. (5), where L_N and L_M are the numbers of degrees of freedom in d space dimensions, e.g. $L_M = \frac{1}{d!}(M+1)\cdot(M+2)\cdot\ldots\cdot(M+d)$. We use the hierarchical orthogonal reconstruction basis functions that are given, e.g. in [14,24], for triangles in 2D and tetrahedrons in 3D. In the following, we will drop the time argument from the notation of the degrees of freedom, meaning $\hat{u}_{pl}^{(m)} = \hat{u}_{pl}^{(m)}(t^n)$ and $\hat{w}_{pl}^{(m)} = \hat{w}_{pl}^{(m)}(t^n)$ for the sake of compactness. In this paper the two operators

$$\langle f, g\rangle = \int_0^1 \int_{T_E} (f(\vec{\xi}, \tau)\cdot g(\vec{\xi}, \tau))\mathrm{d}\vec{\xi}\ \mathrm{d}\tau \qquad [f, g] = \int_{T_E} (f(\vec{\xi}, t)\cdot g(\vec{\xi}, t))\mathrm{d}\vec{\xi} \tag{6}$$

denote, respectively, the scalar products of two functions f and g over the space–time reference element $T_E \times [0;1]$ and the spatial reference element T_E. We choose the functions Φ_l and Ψ_l so as to satisfy the following properties:

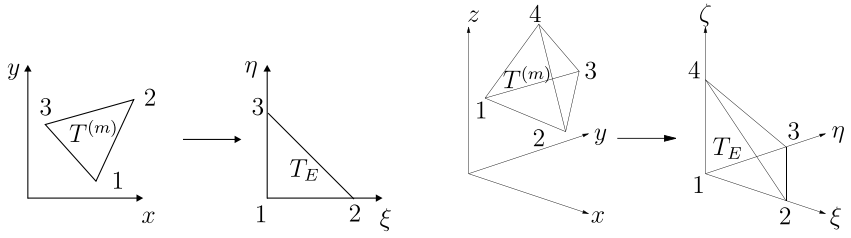

Fig. 2. Transformation from the physical triangle and tetrahedron $T^{(m)}$ to the canonical reference triangle T_E with nodes $(0,0)$, $(1,0)$ and $(0,1)$ and the canonical reference tetrahedron T_E with nodes $(0,0,0)$, $(1,0,0)$, $(0,1,0)$, $(0,0,1)$.

$$\begin{aligned} &\Phi_l = \Psi_l \quad \text{for } 1 \leqslant l \leqslant L_N, \\ &[\Psi_m, \Psi_n] = 0 \quad \forall m,\ \forall n,\ \text{with } m \neq n. \end{aligned} \tag{7}$$

The reconstruction basis functions Ψ_l and the basis functions Φ_l representing the data are equal up to degree N, and the reconstruction basis functions Ψ_l of degree larger than N are chosen to be orthogonal to the Φ_l.

For performing the reconstruction on element $T^{(m)}$, we now choose a reconstruction stencil

$$\mathcal{S}^{(m)} = \bigcup_{k=1}^{n_e} T^{(j(k))} \tag{8}$$

that contains a total number of n_e elements. Here $1 \leqslant k \leqslant n_e$ is a local index, counting the elements in the stencil, and $j = j(k)$ is the mapping from the local index k to the global indexation of the elements in $\mathcal{T}_\Omega$. We set by definition $j(1) = m$ and thus the first element in the stencil ($k = 1$) is always the considered element $T^{(m)}$ for which reconstruction is to be done. For ease of notation, we write in the following only j, meaning $j = j(k)$. The reconstruction technique presented here follows closely the ones presented in [28,29].

We then apply the inverse mapping (3) with respect to element $T^{(m)}$ to all the elements $T^{(j)} \in \mathcal{S}^{(m)}$, where the transformed elements are in the following denoted as $\widetilde{T}^{(j)}$. We emphasize that for all elements $T^{(j)} \in \mathcal{S}^{(m)}$ the mapping with respect to the first element in the stencil is applied, so m is constant for each stencil and therefore the applied mapping formula is the *same* for all elements in $\mathcal{S}^{(m)}$. We note in particular that the transformed element of the first element in the stencil is of course the canonical reference element, hence $\widetilde{T}^{j(1)} = \widetilde{T}^{(m)} = T_E$. The stencil transformed in that way is denoted as $\widetilde{\mathcal{S}}^{(m)} = \bigcup \widetilde{T}^{(j)}$, see examples in [28].

The reconstruction relies on L_2-projection and through the choice of the basis automatically yields a generalized conservation property for all degrees of freedom inside element $T^{(m)}$ up to degree N. In the physical coordinate system we have for each conserved variable u_p

$$\int_{T^{(j)}} \Phi_k \cdot w_p^{(m)}(\vec{\xi}(T^{(m)}, \vec{x}))\mathrm{d}\vec{x} = \int_{T^{(j)}} \Phi_k \cdot u_p^{(j)}(\vec{\xi}(T^{(m)}, \vec{x}))\mathrm{d}\vec{x} \quad \forall T^{(j)} \in \mathcal{S}^{(m)}. \tag{9}$$

Eq. (9) expresses a weak form of the identity of the reconstructed solution w_p of degree M and the original numerical solution u_p of degree N in all elements of the stencil. After transforming all elements of the stencil using (3) and taking into account that the degrees of freedom $\hat{w}_{pl}^{(m)}$ and $\hat{u}_{pl}^{(m)}$ do not depend on space, we obtain the intermediate result

$$|J|\hat{w}_{pl}^{(m)} \int_{\widetilde{T}^{(j)}} \Phi_k \Psi_l \mathrm{d}\vec{\xi} = |J|\hat{u}_{pn}^{(j)} \int_{\widetilde{T}^{(j)}} \Phi_k \Phi_n \,\mathrm{d}\vec{\xi} \quad \forall \widetilde{T}^{(j)} \in \widetilde{\mathcal{S}}^{(m)}.$$

The Jacobian determinant appears on both sides of Eq. (10) and thus cancels out. Please note that this is only possible for triangles and tetrahedrons with straight edges, to which we restrict ourselves in this paper. General polyhedral elements or curved boundaries are not considered here. The canceling of the Jacobian determinants automatically cancels scaling effects of the problem and avoids ill-conditioned reconstruction matrices as reported by Abgrall [1]. During the reconstruction step, the basis polynomials are continuously extended over the whole stencil. In more detail, this extension means that during reconstruction the polynomial term given by $\Psi_l(\vec{\xi})$ is not only valid inside the reference element T_E, but also in all the other elements in the transformed stencil $\widetilde{\mathcal{S}}^{(m)}$. After the reconstructed polynomial for element $T^{(m)}$ has been obtained, the basis polynomials are again restricted to the considered element $T^{(m)}$. We emphasize that the integration on the left-hand side has to be done over the *transformed* elements $\widetilde{T}^{(j)}$. In order to do this integration we perform another coordinate transformation to a second reference coordinate system using the vertices of the transformed element $\widetilde{T}^{(j)}$ as parameter of another mapping from the first $\xi - \eta - \zeta$ reference system to the second $\tilde{\xi} - \tilde{\eta} - \tilde{\zeta}$ reference coordinate system. For convenience, we denote $\vec{\Xi} = (\tilde{\xi}, \tilde{\eta}, \tilde{\zeta})$. The mapping and its inverse are then denoted as

$$\vec{\xi} = \vec{\xi}(\widetilde{T}^{(j)}, \vec{\Xi}), \qquad \vec{\Xi} = \vec{\Xi}(\widetilde{T}^{(j)}, \vec{\xi}) \tag{10}$$

and the Jacobian determinant of this mapping is denoted as $|\widetilde{J}|$. Thus, Eq. (10) becomes after the second transformation

$$\hat{w}_{pl}^{(m)} \int_{T_E} \Phi_k(\vec{\xi}(\widetilde{T}^{(j)}, \vec{\Xi}))\Psi_l(\vec{\xi}(\widetilde{T}^{(j)}, \vec{\Xi}))\mathrm{d}\tilde{\xi}\,\mathrm{d}\tilde{\eta}d\tilde{\zeta} = \hat{u}_{pn}^{(j)} \int_{T_E} \Phi_k(\vec{\xi}(\widetilde{T}^{(j)}, \vec{\Xi}))\Phi_n(\vec{\xi}(\widetilde{T}^{(j)}, \vec{\Xi}))\mathrm{d}\tilde{\xi}\,\mathrm{d}\tilde{\eta}\,\mathrm{d}\tilde{\zeta} \quad \forall \widetilde{T}^{(j)} \in \widetilde{\mathcal{S}}^{(m)}. \tag{11}$$

In order to compute the integral on the left-hand side in (11), we use classical multidimensional Gaussian quadrature of appropriate order. For an exhaustive overview of such multidimensional quadrature formulae see [67]. The integral on the right-hand side is the standard mass-matrix, which is diagonal for the chosen orthogonal basis functions Φ_l.

The reconstruction equations constituted by (11) are solved according to the least squares approach presented in detail in [28]. Here, we indicate only the modifications that have to be carried out. The number of reconstructed degrees of freedom is L_M and per element L_N degrees of freedom are stored. Therefore, we need at least $n_e = \frac{L_M}{L_N}$ elements in each reconstruction stencil. From this expression for n_e it is immediately clear that the reconstructed $P_N P_M$ DG schemes need much smaller stencils than classical finite volume schemes, which makes the $P_N P_M$ schemes very compact for $N > 0$.

On unstructured meshes, we are forced to use *more* elements than the necessary minimum for stability purposes. The use of enlarged reconstruction stencils for robustness purposes has already been reported previously in the literature in the context of finite volume schemes, see e.g. [8,54,49]. We typically choose two times more elements in 2D and three times more but at least 12 elements in 3D. In the general case, the $P_N P_M$ reconstruction leads to very compact stencils, as for HWENO schemes [59,60,5], hence we can admit this quite generous choice for the stencil size. Since (11) becomes overdetermined with the choice $n_e > L_M/L_N$ we use a constrained least-squares technique in order to solve (11) respecting conservation of all degrees of freedom up to degree N in the first element $T^{(m)}$ of the stencil, i.e. we require

$$\hat{w}_{pl}^{(m)} = \hat{u}_{pl}^{(m)} \quad \text{for } 1 \leqslant l \leqslant L_N. \tag{12}$$

Eq. (12) in particular also guarantees conservation of the cell average and Eq. (11) has to be solved with constraint (12) only once for each element in a preprocessing stage and the resulting matrices can be inverted analytically and then stored. The resulting M-exact $P_N P_M$ least squares reconstruction can be interpreted as a generalization of the k-exact reconstruction proposed for pure finite volume schemes by Barth and Frederickson in their pioneering work [8].

From the generalized conservation property (12) and the properties of the reconstruction basis functions (7) we have for all elements $T^{(m)}$ that $w_p = u_p + r_p$ and $r_p \perp u_p$. Hence,

$$[w_p, u_p] = [u_p, u_p]. \tag{13}$$

3. The local space–time continuous Galerkin method

3.1. Review of solution techniques for the high order Riemann problem

Finite volume and discontinuous Galerkin finite element methods make use of numerical fluxes at the interface of each element. The classical method of Godunov [39] computes these fluxes by solving the *classical Riemann problem*, i.e. the Cauchy problem for a system of homogeneous conservation laws, with initial condition consisting of two *constant* states separated by a discontinuity at the origin. In this manner one obtains a first-order accurate method, which is in fact the best first-order method that is also monotone.

Higher-order methods can be constructed by considering higher-order spatial representations of the data, either stemming from a reconstruction procedure as in the finite volume framework, or available directly from a high order polynomial data representation in each element as in the DG framework, or a combination of both, as presented in this paper. This leads in a very natural way to the definition of the high-order Riemann problem (also called the Generalized Riemann problem or the Derivative Riemann Problem). This is the Cauchy problem for the relevant PDEs in which the initial condition consists of two piecewise smooth functions, separated by a discontinuity at the origin.

It appears as if the first author to consider a high-order Riemann problem was Kolgan [50]. He used a monotone piecewise linear polynomial reconstruction, followed by the solution of the classical Riemann problem at the interface for the boundary extrapolated values. Kolgan, however, did not include a local time-evolution of the data, resulting in a linearly unstable method, which is second-order accurate in space, but only first-order accurate in time.

Amongst the many contributions to the subject, since then, there are two main lines of thought. The first is the so-called GRP (Generalized Riemann Problem) method of Ben-Artzi and Falcovitz [9]. They solved the high-order Riemann problem with piecewise linear polynomials, whereby the approximate solution was given as a time power series expansion right at the interface, thus providing a numerical flux for a second-order Godunov-type method.

The other approach of interest is provided by the second-order MUSCL scheme by van Leer [77,78]. This scheme, also attributed by van Leer to Hancock [79], may be viewed as using a solution of the high-order Riemann problem (piece-wise linear polynomial data) that first includes an evolution of the initial condition via the application of the Cauchy–Kovalewski procedure followed by an interaction of the evolved data via a classical Riemann problem solution. Due to the time evolution phase, the MUSCL scheme of van Leer is second-order accurate also in time and linearly stable, in contrast to Kolgan's method.

Extensions of the first approach, that of Ben-Artzi and Falcovitz, were then formulated by several authors such as for example [35,10,36]. These studies were mainly concerned with theoretical aspects of the high-order Riemann problem.

The work of Harten and collaborators [44] may be interpreted as an extension of the second approach, namely the MUSCL scheme of van Leer and Hancock [77–79]. They also evolved the data via the Cauchy–Kovalewski procedure resolving the interaction of the evolved data at the interface via the classical Riemann problem. Harten's work produced fully discrete one step finite volume schemes of theoretically arbitrary order of accuracy in space and time.

In the late 1990s Toro and collaborators returned to the approach of Ben-Artzi and Falcovitz. This effort resulted in what they called ADER schemes [73] (for Arbitrary Accuracy DERivative Riemann problem). These schemes solve the high-order Riemann problem approximately at the interface. For non-linear systems with source terms a semi-analytical solver was first proposed by Toro and Titarev, see [74,71,72]. This solver generalizes the time power series expansion at the interface proposed by Ben-Artzi and Falcovitz. The determination of all the high order terms of the series involves the application of the Cauchy–Kovalewski procedure and the solution of classical linear Riemann problems for the all-order spatial derivatives of the vector of unknowns. The resulting ADER schemes (available for both, the finite volume and the discontinuous Galerkin framework) are, like Harten's schemes, one-step fully discrete and of arbitrary order of accuracy in space and time, see e.g. [73,70,74,64,33,71,72,49,32,68]. The original version of the ADER method, however, needs Gaussian quadrature in space and time in order to compute the fluxes at the interface. In [28,29], the authors proposed a quadrature-free version of the scheme (i.e. not using *numerical* flux integration but *analytical* flux integration at the boundary) of arbitrary accuracy in space and time on unstructured meshes in two and three space dimension. This version of the ADER schemes is more similar to the original ENO scheme proposed by Harten et al., since it first evolves the data in each element via the Cauchy–Kovalewski procedure and then solves the interactions at the boundary. To obtain a quadrature-free version of the scheme, all the space–time information produced by the Cauchy–Kovalewski procedure has been used, which was neither done in the original ENO scheme of Harten et al. nor in previous ADER schemes. For DG schemes, a very efficient fully discrete Cauchy–Kovalewski based approach, similar to the one of Harten *et al.* [44], has been introduced recently in [53,37].

In a recent paper, Castro and Toro [12] have re-interpreted the schemes of van Leer and Harten et al. in the framework of the solution of the high-order Riemann problem at the interface and systematically compared various different possible semi-analytical methods based on the Cauchy–Kovalewski procedure for solving the high-order Riemann problem. They found that for linear hyperbolic systems, all approaches coincide.

We note that the main inconvenience induced by the Cauchy–Kovalewski procedure is that it may quickly become very complex for general hyperbolic systems in multiple space dimensions and at higher order of accuracy, although for very important systems like the Euler [32,29], MHD [68] and Navier–Stokes [37] equations this procedure is available for any order of accuracy due to modifications of a semi-analytic algorithm originally developed by Dyson [34].

An alternative solver for the high-order Riemann problem has recently been proposed by Dumbser et al. [26]. This is an entirely numerical solver that starts from the Harten approach of evolving the data inside each element in a predictor step. But instead of using the *strong, differential, form* of the governing PDE for data evolution, i.e. instead of using the semi-analytical Cauchy–Kovalewski method, the *weak, integral, form* of the

governing PDE in space–time is used to evolve the data numerically. This is done using a new *local* space–time discontinuous Galerkin approach, different from the global space–time DG schemes introduced by van der Vegt and van der Ven [75,76]. The local space–time approach presented in [26] results in *small local* nonlinear algebraic systems to be solved, compared to the globally implicit formulation of the space–time DG approach presented in [75,76]. Then, the interaction of the evolved data at the desired time $t = \tau$ requires the solution of the classical Riemann problem. The advantages of this numerical variant are twofold: (i) one avoids completely the cumbersome Cauchy–Kovalewski procedure, resulting in great generality and (ii) one can treat stiff source terms properly, reconciling the usually incompatible concepts of high accuracy and stiffness.

Although the new local space–time DG scheme presented in [26] is very successful for stiff problems and also applicable to very general hyperbolic systems, it is computationally more expensive compared to the Cauchy–Kovalewski procedure. In the space–time DG framework [75,76] the initial condition is imposed only in a weak form, which leads to a large number of degrees of freedom to solve for. For non-stiff problems, the extra degrees of freedom allowing the numerical solution of the local space–time DG scheme to be different at time $t = 0^+$ from the initial condition at time $t = 0$ are not important, since for non-stiff problems the numerical solution will usually exhibit only very small jumps between $t = 0$ and $t = 0^+$. Therefore, we now propose to use a *local continuous* space–time Galerkin machinery to evolve the data inside each element in order to obtain smaller algebraic systems that, as has turned out in our research, can be solved very efficiently by a simple iteration scheme.

3.2. Weak local space–time formulation

In this article we consider nonlinear time-dependent hyperbolic systems of conservation laws of the form

$$\frac{\partial}{\partial t}u_p + \frac{\partial}{\partial x}f_p + \frac{\partial}{\partial y}g_p + \frac{\partial}{\partial z}h_p = S_p, \tag{14}$$

where u_p is the vector of conserved variables, $f_p = f_p(u_q)$, $g_p = g_p(u_q)$ and $h_p = h_p(u_q)$ are the nonlinear fluxes and $S_p = S_p(u_q)$ is a nonlinear but non-stiff algebraic source term. In this paper, only the non-stiff case is considered, for the robust and accurate treatment of stiff sources we refer the reader to [26]. Introducing the local time $\tau = (t - t^n)/\Delta t$ and the coordinate transformation (3), we first rewrite the governing PDE (14) in the reference coordinates ξ, η, ζ and τ as

$$\frac{\partial}{\partial \tau}u_p + \frac{\partial}{\partial \xi}f_p^* + \frac{\partial}{\partial \eta}g_p^* + \frac{\partial}{\partial \zeta}h_p^* = S_p^* \tag{15}$$

with

$$\begin{aligned} &f_p^* = \Delta t(f_p\xi_x + g_p\xi_y + h_p\xi_z), \quad g_p^* = \Delta t(f_p\eta_x + g_p\eta_y + h_p\eta_z), \quad h_p^* = \Delta t(f_p\zeta_x + g_p\zeta_y + h_p\zeta_z), \\ &S_p^* = \Delta t S_p. \end{aligned} \tag{16}$$

We now multiply (15) with space and time dependent test functions $\theta_k = \theta_k(\vec{\xi}, \tau)$ and integrate over the space–time reference element $T_E \times [0;1]$:

$$\left\langle \theta_k, \frac{\partial}{\partial \tau}u_p \right\rangle + \left\langle \theta_k, \frac{\partial}{\partial \xi}f_p^* \right\rangle + \left\langle \theta_k, \frac{\partial}{\partial \eta}g_p^* \right\rangle + \left\langle \theta_k, \frac{\partial}{\partial \zeta}h_p^* \right\rangle = \langle \theta_k, S_p^* \rangle. \tag{17}$$

The numerical solution of (17) in space–time, denoted by $\mathcal{U}_p$, as well as the fluxes and the source terms are approximated using the same space–time basis functions θ_k as used for the test functions, i.e.

$$\begin{aligned} &\mathcal{U}_p(\vec{\xi}, \tau) = \widehat{\mathcal{U}}_{lp}\theta_l(\vec{\xi}, \tau), \quad \mathcal{S}_p(\vec{\xi}, \tau) = \widehat{\mathcal{S}}_{lp}\theta_l(\vec{\xi}, \tau), \quad \mathcal{F}_p(\vec{\xi}, \tau) = \widehat{\mathcal{F}}_{lp}\theta_l(\vec{\xi}, \tau), \\ &\mathcal{G}_p(\vec{\xi}, \tau) = \widehat{\mathcal{G}}_{lp}\theta_l(\vec{\xi}, \tau), \quad \mathcal{H}_p(\vec{\xi}, \tau) = \widehat{\mathcal{H}}_{lp}\theta_l(\vec{\xi}, \tau), \end{aligned} \tag{18}$$

where we use classical tensor index notation, implying summation over indices appearing twice. For the degrees of freedom, the same transformation (16) for the fluxes and source terms holds, i.e.

$$\widehat{\mathcal{F}}^*_{lp} = \Delta t(\widehat{\mathcal{F}}_{lp}\xi_x + \widehat{\mathcal{G}}_{lp}\xi_y + \widehat{\mathcal{H}}_{lp}\xi_z), \quad \widehat{\mathcal{G}}^*_{lp} = \Delta t(\widehat{\mathcal{F}}_{lp}\eta_x + \widehat{\mathcal{G}}_{lp}\eta_y + \widehat{\mathcal{H}}_{lp}\eta_z),$$
$$\widehat{\mathcal{H}}^*_{lp} = \Delta t(\widehat{\mathcal{F}}_{lp}\zeta_x + \widehat{\mathcal{G}}_{lp}\zeta_y + \widehat{\mathcal{H}}_{lp}\zeta_z), \quad \widehat{\mathcal{S}}^*_{lp} = \Delta t\widehat{\mathcal{S}}_{lp}. \tag{19}$$

Inserting (18) into (17) yields

$$\left\langle \theta_k, \frac{\partial}{\partial\tau}\theta_l \right\rangle \widehat{\mathcal{U}}_{lp} + \left\langle \theta_k, \frac{\partial}{\partial\xi}\theta_l \right\rangle \widehat{\mathcal{F}}^*_{lp} + \left\langle \theta_k, \frac{\partial}{\partial\eta}\theta_l \right\rangle \widehat{\mathcal{G}}^*_{lp} + \left\langle \theta_k, \frac{\partial}{\partial\zeta}\theta_l \right\rangle \widehat{\mathcal{H}}^*_{lp} = \langle \theta_k, \theta_l \rangle \widehat{\mathcal{S}}^*_{lp}. \tag{20}$$

The matrices arising in equation system (20) are the temporal stiffness matrix K^{τ}_{kl}, the mass matrix M_{kl} and the spatial stiffness matrices K^{ξ}_{kl}, K^{η}_{kl} and K^{ζ}_{kl}, defined as follows:

$$K^{\tau}_{kl} = \left\langle \theta_k, \frac{\partial}{\partial\tau}\theta_l \right\rangle, \quad M_{kl} = \langle \theta_k, \theta_l \rangle, \quad K^{\xi}_{kl} = \left\langle \theta_k, \frac{\partial}{\partial\xi}\theta_l \right\rangle, \quad K^{\eta}_{kl} = \left\langle \theta_k, \frac{\partial}{\partial\eta}\theta_l \right\rangle, \quad K^{\zeta}_{kl} = \left\langle \theta_k, \frac{\partial}{\partial\zeta}\theta_l \right\rangle. \tag{21}$$

We still need a relation between the degrees of freedom $\widehat{\mathcal{U}}_{lp}$ of the numerical solution, the degrees of freedom $\widehat{\mathcal{F}}_{lp}$, $\widehat{\mathcal{G}}_{lp}$ and $\widehat{\mathcal{H}}_{lp}$ approximating the fluxes and $\widehat{\mathcal{S}}_{lp}$ approximating the source. The best one would be an L^2 projection but this would involve the numerical computation of space–time integrals with very high order of accuracy, which may become prohibitively expensive for time dependent problems in three space dimensions. Therefore we prefer to use a *nodal approach* where the degrees of freedom of the fluxes and the source term are simply evaluated as the physical fluxes and the source at the respective degrees of freedom of the state $\widehat{\mathcal{U}}_{pl}$:

$$\widehat{\mathcal{F}}_{lp} = f_p(\widehat{\mathcal{U}}_{lq}), \quad \widehat{\mathcal{G}}_{lp} = g_p(\widehat{\mathcal{U}}_{lq}), \quad \widehat{\mathcal{H}}_{lp} = h_p(\widehat{\mathcal{U}}_{lq}), \quad \widehat{\mathcal{S}}_{lp} = S_p(\widehat{\mathcal{U}}_{lq}). \tag{22}$$

All the stiffness matrices defined in (21) are singular, which is physically correct because we still have to introduce the initial condition at $\tau = 0$ into Eq. (20). If we construct our nodal basis functions θ_l in such a way that the first degrees of freedom are located at different spatial points at relative time $\tau = 0$, grouped together in a sub-vector $\widehat{\mathcal{U}}^0_{lp}$, and all the other degrees of freedom are located at spatial points at later times $\tau > 0$, grouped together in a sub-vector $\widehat{\mathcal{U}}^1_{lp}$, we can write the total vector of degrees of freedom as $\widehat{\mathcal{U}}_{lp} = (\widehat{\mathcal{U}}^0_{lp}, \widehat{\mathcal{U}}^1_{lp})^{\mathrm{T}}$. The same holds for the fluxes and the source term, i.e. $\widehat{\mathcal{F}}^*_{lp} = (\widehat{\mathcal{F}}^0_{lp}, \widehat{\mathcal{F}}^1_{lp})^T$, $\widehat{\mathcal{G}}^*_{lp} = (\widehat{\mathcal{G}}^0_{lp}, \widehat{\mathcal{G}}^1_{lp})^{\mathrm{T}}$, $\widehat{\mathcal{H}}^*_{lp} = (\widehat{\mathcal{H}}^0_{lp}, \widehat{\mathcal{H}}^1_{lp})^{\mathrm{T}}$ and $\widehat{\mathcal{S}}^*_{lp} = (\widehat{\mathcal{S}}^0_{lp}, \widehat{\mathcal{S}}^1_{lp})^{\mathrm{T}}$. According to this definition, we introduce the following sub-matrix notation for the mass matrix and the stiffness matrices, where α may represent τ, ξ, η or ζ, respectively,

$$\underline{\underline{M}} = \begin{pmatrix} \underline{\underline{M}}^{00} & \underline{\underline{M}}^{01} \\ \underline{\underline{M}}^{10} & \underline{\underline{M}}^{11} \end{pmatrix}, \qquad \underline{\underline{K}}^{\alpha} = \begin{pmatrix} \underline{\underline{K}}^{\alpha,00} & \underline{\underline{K}}^{\alpha,01} \\ \underline{\underline{K}}^{\alpha,10} & \underline{\underline{K}}^{\alpha,11} \end{pmatrix}. \tag{23}$$

Note that the degrees of freedom of the state at relative time $\tau = 0$ are *known* from the reconstruction polynomials $w_p(\vec{\xi}, t^n)$ and due to Eq. (22) also the degrees of freedom of the fluxes and the source term at $\tau = 0$ are known. Removing test functions of known degrees of freedom (i.e. canceling the first rows of the equation system) and moving the degrees of freedom known from the initial condition onto the right-hand side of the equation system we obtain from (20):

$$\begin{aligned} &K^{\tau,11}_{kl}\widehat{\mathcal{U}}^1_{lp} + K^{\xi,11}_{kl}\widehat{\mathcal{F}}^1_{lp} + K^{\eta,11}_{kl}\widehat{\mathcal{G}}^1_{lp} + K^{\zeta,11}_{kl}\widehat{\mathcal{H}}^1_{lp} - M^{11}_{kl}\mathcal{S}^1_{lp} \\ &\quad = -K^{\tau,10}_{kl}\widehat{\mathcal{U}}^0_{lp} - K^{\xi,10}_{kl}\widehat{\mathcal{F}}^0_{lp} - K^{\eta,10}_{kl}\widehat{\mathcal{G}}^0_{lp} - K^{\zeta,10}_{kl}\widehat{\mathcal{H}}^0_{lp} + M^{10}_{kl}\widehat{\mathcal{S}}^0_{lp}. \end{aligned} \tag{24}$$

Eq. (24) together with (22) form a nonlinear algebraic system for the unknowns $\widehat{\mathcal{U}}^1_{lp}$ on the left-hand side and all quantities with the superscript '0' on the right-hand side are known from the initial condition at $\tau = 0$. We propose to use the following iterative approach: the temporal stiffness matrix $K^{\tau,11}_{kl}$ is universal and does neither depend on the mesh nor on the timestep nor on the equations to be solved. For all orders of accuracy and for all numbers of space dimensions treated in this paper, it also could be inverted analytically and therefore we obtain the following simple iteration scheme for $\widehat{\mathcal{U}}^1_{lp}$, where the superscript 'i' denotes the iteration number:

$$\begin{aligned} \widehat{\mathcal{U}}^{1,i+1}_{lp} &= (K^{\tau,11}_{lk})^{-1}(M^{11}_{kn}\widehat{\mathcal{S}}^{1,i}_{np} - K^{\xi,11}_{kn}\widehat{\mathcal{F}}^{1,i}_{np} - K^{\eta,11}_{kn}\widehat{\mathcal{G}}^{1,i}_{np} - K^{\zeta,11}_{kn}\widehat{\mathcal{H}}^{1,i}_{np}) \\ &\quad + (K^{\tau,11}_{lk})^{-1}(M^{10}_{kn}\widehat{\mathcal{S}}^{0}_{np} - K^{\xi,10}_{kn}\widehat{\mathcal{F}}^{0}_{np} - K^{\eta,10}_{kn}\widehat{\mathcal{G}}^{0}_{np} - K^{\zeta,10}_{kn}\widehat{\mathcal{H}}^{0}_{np} - K^{\tau,10}_{kn}\widehat{\mathcal{U}}^{0}_{np}) \end{aligned} \tag{25}$$

Using symbolic linear algebra tools, we found *analytically* some very interesting properties of the matrices

$$A_\xi := (K_{lk}^{\tau,11})^{-1} K_{kn}^{\xi,11}, \quad A_\eta := (K_{lk}^{\tau,11})^{-1} K_{kn}^{\eta,11}, \quad A_\zeta := (K_{lk}^{\tau,11})^{-1} K_{kn}^{\zeta,11}, \tag{26}$$

using the space–time basis functions presented in Section 3.3. Although the matrices are almost fully populated, *all* the eigenvalues of these matrices are zero, for *any* order of accuracy up to six and for *any* number of space dimensions up to three. Furthermore, also all the matrices formed by an arbitrary linear combination $\omega_1 A_\xi + \omega_2 A_\eta + \omega_3 A_\zeta$ of these matrices have only eigenvalues that are all zero. We conjecture, that this holds for any order and any number of space dimensions. Furthermore, the absolute values of all eigenvalues of the matrix $(K_{lk}^{\tau,11})^{-1} M_{kn}^{11}$ are less than one. At least for linear hyperbolic PDE, this automatically implies directly that the operator (25) is a *contraction* and therefore the scheme (25) is a contractive fixed point iteration. According to the Banach fixed point theorem, the iterative scheme (25) therefore has a unique solution and the convergence of the method to this solution is guaranteed, at least under a suitable CFL stability condition. For linear homogeneous scalar equations we furthermore observed (using analytical computations via symbolic algebra tools) that the method always converges for *any* initial guess vector after at most M iterations. We think that the method (25) can be directly interpreted as a discrete analogue of the Picard iteration for ODEs, see [52,81], since the matrix $K_{lk}^{\tau,11}$ is a discrete derivative operator in time and hence its inverse matrix $(K_{lk}^{\tau,11})^{-1}$ represents a discrete time integration operator.

The iterative scheme (25) is very simple, robust and efficient. As an initial guess value for $\widehat{U}_{lp}^{1}$ we suppose a stationary solution of the PDE (15) to begin with. From the extensive numerical experiments shown later in Section 6 of this paper we found that also for nonlinear systems only at most M or $M+1$ iterations were needed to reach convergence to a precision of 10^{-9} using the iterative scheme (25). Our observation is furthermore supported by the error estimate given in [81] for the continuous Picard iteration, which states that the error is of the order $\mathcal{O}(\Delta t^{M+1})$ after M iterations. We remark that due to the structure of the equation system (24), the second-order local space–time Galerkin schemes are fully explicit and hence do not need any iteration. In the second-order finite volume case, the method automatically reduces to the MUSCL scheme. Since (25) is based on a weak formulation of the PDE using a nodal space–time finite element approach, only evaluations of physical fluxes and source terms are required and no differentiation operations are needed, compared to the rather complicated Cauchy–Kovalewski procedure used in the original ENO scheme [44] as well as in previous ADER schemes [29,31,32,68,71,74] and other Cauchy–Kovalewski based methods [58,57,53,37]. Thus, (25) is very general and can be applied also to complex hyperbolic systems such as nonlinear elasticity and relativistic magnetohydrodynamics, as seen later in Section 6.

3.3. Choice of the space–time basis

As already mentioned in the previous section the optimal way to connect the space–time degrees of freedom for the fluxes and the source term with those of the vector of conserved variables would be an L^2 projection. However, this would become prohibitively expensive in three space dimensions plus time. Therefore, a nodal approach is chosen, leading to (22), where we take special care of using the minimal number of space–time nodes necessary to reach the formal order of accuracy. In d space dimensions, the optimal number of space–time degrees of freedom for a $P_N P_M$ scheme with reconstruction polynomial degree M is

$$n_{\mathrm{DOF}}^{\mathrm{ST}}(d,M) = \frac{1}{(d+1)!} \prod_{j=1}^{d+1} (M+j). \tag{27}$$

The only restriction concerning the distribution of the nodes is that we have a sufficient number of nodes located at $\tau = 0$ to include the initial condition. The minimum number of nodes at $\tau = 0$ is therefore $n_{\mathrm{DOF}}^{\mathrm{ST}}(d-1,M)$. We choose the following simple distributions in one space dimension, on triangles in two space dimension and on tetrahedra in three space dimensions:

$$(\xi_{kl},\tau_{kl}) = \left(\frac{k}{M-l},\frac{l}{M}\right), \tag{28}$$

$$(\xi_{jkl},\eta_{jkl},\tau_{jkl}) = \left(\frac{j}{M-l},\frac{k}{M-l},\frac{l}{M}\right), \tag{29}$$

$$(\xi_{ijkl},\eta_{ijkl},\zeta_{ijkl},\tau_{ijkl}) = \left(\frac{i}{M-l},\frac{j}{M-l},\frac{k}{M-l},\frac{l}{M}\right)$$
$$\text{for } 0 \leqslant l < M, \quad 0 \leqslant k \leqslant M-l, \quad 0 \leqslant j \leqslant M-l-k, \quad 0 \leqslant i \leqslant M-l-k-j. \tag{30}$$

The last point, corresponding to the singular case $l = M$ in Eqs. (28)–(30), is inserted at the spatial barycenter of the reference element at $\tau = 1$, i.e.:

$$(\vec{\xi}_{0\ldots0M},\tau_{0\ldots0M}) = \left(\frac{1}{d+1},\ldots,\frac{1}{d+1},1\right). \tag{31}$$

In Figs. 3 and 4 we show the nodal distribution for a fourth-order local space–time continuous Galerkin scheme in one space dimension and for a triangle in two space dimensions, respectively.

4. Formulation of the fully-discrete quadrature-free $P_N P_M$ DG schemes for general nonlinear hyperbolic systems

To derive the fully discrete form of the $P_N P_M$ schemes we multiply the conservation law (14) with a test function Φ_k and integrate over the space–time element $T^{(m)} \times [t^n; t^n + \Delta t]$, using integration by parts in space:

$$\int_{t^n}^{t^n+\Delta t}\int_{T^{(m)}} \Phi_k \frac{\partial}{\partial t} u_p \,\mathrm{d}V\,\mathrm{d}t + \int_{t^n}^{t^n+\Delta t}\int_{\partial T^{(m)}} \Phi_k \vec{F}_p\cdot\vec{n}\,\mathrm{d}S\,\mathrm{d}t - \int_{t^n}^{t^n+\Delta t}\int_{T^{(m)}} \frac{\partial \Phi_k}{\partial \vec{x}}\cdot\vec{F}_p\,\mathrm{d}V\,\mathrm{d}t = \int_{t^n}^{t^n+\Delta t}\int_{T^{(m)}} \Phi_k S_p\,\mathrm{d}V\,\mathrm{d}t, \tag{32}$$

with $\vec{F}_p = (f_p,\ g_p,\ h_p)$ and $\partial\Phi_k/\partial\vec{x} = \left(\frac{\partial\Phi_k}{\partial x},\frac{\partial\Phi_k}{\partial y},\frac{\partial\Phi_k}{\partial z}\right)$. Furthermore, $\vec{n} = (n_x, n_y, n_z)^T$ is the outward pointing unit normal vector on the surface $\partial T^{(m)}$ of the element. In classical DG schemes [18,17,15,13,20] the fluxes and source terms in (32) are computed using the same piecewise polynomials of degree N as used for the representation of the numerical solution u_p, i.e. $\vec{F}_p := \vec{F}_p(u_q)$ and $S_p := S_p(u_q)$. In this paper we propose to use instead the solution of the local space–time Galerkin scheme (24) with polynomial degree M to compute the fluxes and source terms in (32), i.e. we use $\vec{F}_p := \vec{\mathcal{F}}_p = (\mathcal{F}_p, \mathcal{G}_p, \mathcal{H}_p)^{\mathrm{T}}$ and $S_p := \mathcal{S}_p$. To define the surface integral a numerical flux must be introduced. Since we want to construct quadrature-free schemes, it is natural to use also the space–time solution obtained for the fluxes from (24). We therefore use the four-argument flux function $\vec{F}^h_p = \vec{F}^h_p(\mathcal{U}^-_q, \mathcal{U}^+_q, \vec{\mathcal{F}}^-_q, \vec{\mathcal{F}}^+_q)$ introduced in [29], which allows an *analytical* integration over the element boundaries. It consists of a classical two-point interface flux $\vec{F}^{(L)}_p$ as a leading flux, which depends only on the left and right states at the space–time barycenter of each element interface, and a four-argument corrector flux $\vec{F}^{(C)}_p$ that takes into account the whole polynomial space–time representation of the states on the left and right of the interface and which is a *linear* function in its arguments and hence allows analytical integration:

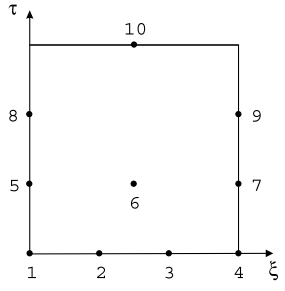

Fig. 3. Distribution of the space–time nodes for the fourth-order local space–time continuous Galerkin scheme in one space dimension plus time.

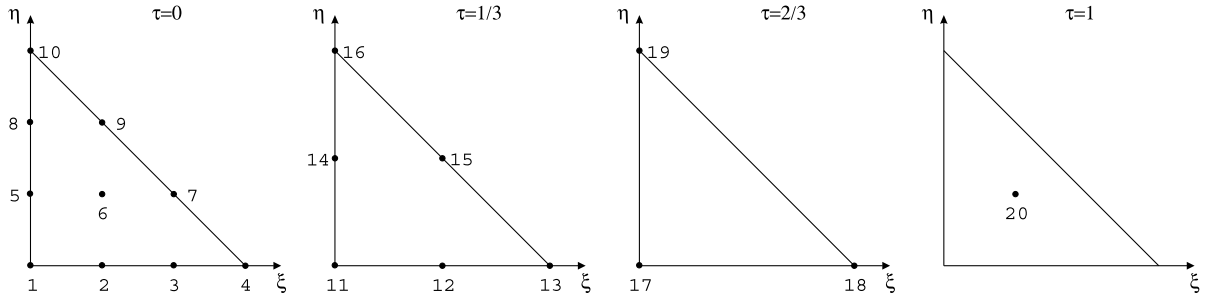

Fig. 4. Distribution of the space–time nodes for the fourth-order local space–time continuous Galerkin scheme in two space dimensions plus time.

$$\vec{F}_p^h(\mathcal{U}_q^-,\mathcal{U}_q^+,\vec{\mathcal{F}}_q^-,\vec{\mathcal{F}}_q^+) = \vec{F}_p^{(L)}(\mathcal{U}_q^-(\vec{\xi}(\bar{\chi}_1,\bar{\chi}_2),\bar{\tau}),\mathcal{U}_q^+(\vec{\xi}(\bar{\chi}_1,\bar{\chi}_2),\bar{\tau})) + \vec{F}_p^{(C)}(\mathcal{U}_q^-,\mathcal{U}_q^+,\vec{\mathcal{F}}_q^-,\vec{\mathcal{F}}_q^+). \tag{33}$$

Here, $\bar{\chi}_1$, $\bar{\chi}_2$ and $\bar{\tau}$ denote the space–time barycenter of the element face. In this paper, we decide to choose the Rusanov flux as leading and corrector flux due to its simplicity, robustness and generality. As described in detail in [29] the signal velocities are once computed using the states at the element face space–time barycenter and then are frozen, i.e. kept constant, for the whole face inside the corrector flux.

Integrating the first term in (32) in space and time, introducing the numerical flux, and rewriting the third term over the space–time reference element $T_E \times [0;1]$ we get the following expression of our fully discrete one-step $P_N P_M$ schemes:

$$\begin{aligned}&[\Phi_k,\Phi_l](\hat{u}_{lp}^{n+1}-\hat{u}_{lp}^{n}) + \frac{\Delta t}{|J|}\int_0^1\int_{\partial T^{(m)}} \Phi_k \vec{F}_p^h(\mathcal{U}_q^-,\mathcal{U}_q^+,\vec{\mathcal{F}}_q^-,\vec{\mathcal{F}}_q^+)\cdot\vec{n}\,\mathrm{d}S\,\mathrm{d}\tau \\ &-\left(\left\langle\frac{\partial\Phi_k}{\partial\xi},\mathcal{F}_p^*\right\rangle + \left\langle\frac{\partial\Phi_k}{\partial\eta},\mathcal{G}_p^*\right\rangle + \left\langle\frac{\partial\Phi_k}{\partial\zeta},\mathcal{H}_p^*\right\rangle\right) = \langle\Phi_k,\mathcal{S}_p^*\rangle.\end{aligned} \tag{34}$$

Note that the local space–time Galerkin solution $\mathcal{U}_p$ as well as the resulting fluxes $\mathcal{F}_p$, $\mathcal{G}_p$, $\mathcal{H}_p$ and the source term $\mathcal{S}_p$ are related to the reconstructed solution $w_p = w_p(\vec{\xi},t^n)$ of degree M at time t^n via the local space–time continuous Galerkin scheme (24) and the reconstructed solution w_p at time t^n is related to the original numerical solution u_p of (34) via the reconstruction operator (11) and the generalized conservation property (12), i.e. we have the dependency $\mathcal{U}_p = \mathcal{U}_p(w_q(u_r))$ and similarly also for the fluxes and source terms. Note that a pure DG scheme is recovered by setting $N = M$, i.e. $w_p = u_p$ and the pure finite volume case is obtained by setting $N = 0$, i.e. the $\hat{u}_{lp}$ reduce to the cell averages $\bar{u}_p$.

Due to the linearity of the corrector flux in its four arguments, flux computation and space–time integration can be exchanged. To perform this integration analytically, we introduce the following mesh-independent flux matrices, which can be precomputed once and then stored:

$$F_k^{0,e} = \int_0^1\int_{\partial(T_E)_e} \Phi_k\,\mathrm{d}\chi_1\,\mathrm{d}\chi_2\,\mathrm{d}\tau, \tag{35}$$

$$F_{kl}^{-,e} = \int_0^1\int_{\partial(T_E)_e} \Phi_k(\theta_l(\vec{\xi}^{(e)}(\chi_1,\chi_2),\tau) - \theta_l(\vec{\xi}^{(e)}(\bar{\chi}_1,\bar{\chi}_2),\bar{\tau}))\mathrm{d}\chi_1\,\mathrm{d}\chi_2\,\mathrm{d}\tau, \tag{36}$$

$$F_{kl}^{+,e^+,h} = \int_0^1\int_{\partial(T_E)_e} \Phi_k(\theta_l(\vec{\xi}^{(e^+)}(\tilde{\chi}_1^{(h)},\tilde{\chi}_2^{(h)}),\tau) - \theta_l(\vec{\xi}^{(e^+)}(\bar{\chi}_1,\bar{\chi}_2),\bar{\tau}))\mathrm{d}\chi_1\,\mathrm{d}\chi_2\,\mathrm{d}\tau. \tag{37}$$

Here, e and e^+ are the local numbers of the considered common element interface between element $T^{(m)}$ and its neighbor element $T^{(k_e)}$ as seen from each element, respectively, and h takes into account the possibly different orientations of two tetrahedral faces due to rotation and has a meaning only in the three-dimensional case. The element faces are parametrized by the face parameters χ_1 and χ_2, which are mapped to the volume coordinates $\vec{\xi}$ by a mapping function depending on the face number and the orientation. We furthermore use the notation $\Phi_k = \Phi_k((\vec{\xi}^{(e)}(\chi_1,\chi_2)))$. For more details on the computation of the flux matrices in 2D and 3D, see

[28] and [29]. The final form of the fully discrete scheme using the definition of the flux-matrices introduced above yields

$$
\begin{aligned}
&[\Phi_k,\Phi_l](\hat{u}_{lp}^{n+1}-\hat{u}_{lp}^{n})+\sum_{e=1}^{N_E}\Delta t\frac{|J_{\partial T_e}|}{|J|}(F_k^{0,e}\vec{F}_p^{(L)}+\vec{F}_p^{(C)}(F_{kl}^{-,e}\widehat{\mathcal{U}}_{lq}^{-},F_{kl}^{+,e^+,h}\widehat{\mathcal{U}}_{q}^{+},F_{kl}^{-,e}\vec{\widehat{\mathcal{F}}}_{lq}^{-},F_{kl}^{+,e^+,h}\vec{\widehat{\mathcal{F}}}_{q}^{+}))\cdot\vec{n}_e\\
&-\left(\left\langle\frac{\partial\Phi_k}{\partial\xi},\theta_l\right\rangle\widehat{\mathcal{F}}_{lp}^{*}+\left\langle\frac{\partial\Phi_k}{\partial\eta},\theta_l\right\rangle\widehat{\mathcal{G}}_{lp}^{*}+\left\langle\frac{\partial\Phi_k}{\partial\zeta},\theta_l\right\rangle\widehat{\mathcal{H}}_{lp}^{*}\right)\\
&=\langle\Phi_k,\theta_l\rangle\widehat{\mathcal{S}}_{lp}^{*}.
\end{aligned}
\tag{38}
$$

In the following, we summarize the necessary steps of the whole algorithm described in this section to perform the update of the degrees of freedom $\hat{u}_{lp}$ from time t^n to time $t^n+\Delta t$:

(1) *Reconstruction*. Apply the P_NP_M reconstruction algorithm described in Section 2 to the numerical solution u_p at time t^n represented by the piecewise polynomials of degree N to obtain the higher order reconstruction polynomials w_p of degree M, i.e. compute $\hat{w}_{lp}=\hat{w}_{lp}(\hat{u}_{mq}^{n})$.
(2) *Local data evolution*. Use the reconstructed solution w_p in each element as initial condition for the local continuous space–time Galerkin method presented in Section 3. Solve for $\mathcal{U}_p$ via the iterative scheme (25) to obtain $\widehat{\mathcal{U}}_{lp}=\widehat{\mathcal{U}}_{lp}(\hat{w}_{mq})$, $\widehat{\mathcal{F}}_{lp}=\widehat{\mathcal{F}}_{lp}(\hat{w}_{mq})$, $\widehat{\mathcal{G}}_{lp}=\widehat{\mathcal{G}}_{lp}(\hat{w}_{mq})$, $\widehat{\mathcal{H}}_{lp}=\widehat{\mathcal{H}}_{lp}(\hat{w}_{mq})$ and $\widehat{\mathcal{S}}_{lp}=\widehat{\mathcal{S}}_{lp}(\hat{w}_{mq})$.
(3) *Solution of the Riemann Problem*. Solve the Riemann problem at the interface approximately using the space–time polynomials of the state, the fluxes and the source terms generated in the previous step. A quadrature-free flux integral can be obtained using the special four-argument numerical flux function introduced in [28].
(4) *Update*. Update the degrees of freedom $\hat{u}_{lp}$ from time level n to time level $n+1$ according to the quadrature-free formulation (38).

5. Linear stability analysis and numerical convergence studies

5.1. von-Neumann stability analysis

To assess the stability of the proposed P_NP_M schemes we perform a von-Neumann stability analysis, see e.g. [45] for details, applying the schemes to the linear scalar advection equation in one space dimension

$$
\frac{\partial u}{\partial t}+a\frac{\partial u}{\partial x}=0,\qquad a\in\mathbb{R},\ \ a>0.
\tag{39}
$$

As usual for a von-Neumann analysis, we suppose an equidistant partition of a periodic computational domain $\Omega=\bigcup T^j$ with element length Δx, where the degrees of freedom of the numerical solution of (39) at time t^n are written for each element T^j in terms of a single vector Fourier mode of the form

$$
\hat{u}_l^j(t^n)=\widetilde{U}_l^n\mathrm{e}^{\mathrm{i}kj\Delta x}
\tag{40}
$$

with the amplitude vector $\widetilde{U}_l^n$ at time t^n, the wavenumber k and the imaginary unit $\mathrm{i}^2=-1$. Applying the linear P_NP_M reconstruction operator proposed in Section 2 to the degrees of freedom (40) we obtain a Fourier mode representation for the degrees of freedom of the reconstructed solution as $\hat{w}_l^j(t^n)=\widetilde{W}_l^n(\widetilde{U}_l^n,k)\mathrm{e}^{\mathrm{i}kj\Delta x}$, where the amplitude vector $\widetilde{W}_l^n=\widetilde{W}_l^n(\widetilde{U}_l^n,k)$ is a function of the amplitude vector $\widetilde{U}_l^n$ and the wavenumber k. It depends on the reconstruction operator and its expression is quite complicated, but it can be computed using modern computer algebra systems. Finally, the time discretization technique introduced by the local space–time continuous Galerkin methods proposed in Section 3 is applied and the result for the space–time degrees of freedom $\widehat{\mathcal{U}}_l^j$ is inserted into the fully discrete one-step scheme (38). Then, the amplification factor matrix G_{ml}, which is a function of the Courant number $\mathrm{CFL}=a\Delta t/\Delta x$ and the reduced wavenumber $\varphi=k\Delta x$ can be determined from the relation $\widetilde{U}_m^{n+1}=G_{ml}(\varphi,\mathrm{CFL})\widetilde{U}_l^n$. The eigenvalues of G_{ml} are then computed numerically. The method is stable if the largest eigenvalue of G_{ml} is less than one for all reduced wavenumbers $0<\varphi<\pi$. The maximum admissible Courant numbers for all possible P_NP_M schemes up to fifth-order of

Table 1
Stability limits for $P_N P_M$ schemes from second- to fifth-order of accuracy

CFL_{max}	$N = 0$	$N = 1$	$N = 2$	$N = 3$	$N = 4$
$M = 1$	1.00	0.33			
$M = 2$	1.00	0.32	0.17		
$M = 3$	1.00	0.32	0.17	0.10	
$M = 4$	1.00	0.32	0.17	0.10	0.069

accuracy in space and time are given in Table 1. From these results we can deduce that it is the polynomial degree N of the data representation that governs the stability of the method and *not* the polynomial degree M of the reconstruction operator. Hence, the new class of schemes with $N > 0$ and $M > N$ allows for larger time steps than the pure DG method of the same order.

5.2. Numerical convergence studies on unstructured meshes

5.2.1. Two-dimensional Euler equations

The convergence studies of the two-dimensional version of our $P_N P_M$ schemes are carried out solving the Euler equations of compressible gas dynamics, with conservative variables $u_p = (\rho, \rho v_j, \rho E)^T$ and the flux tensor defined as

$$\vec{F}_p = F_{pi} = \begin{pmatrix} \rho v_i \\ \rho v_i v_j + p\ \delta_{ij} \\ v_i(\rho E + p) \end{pmatrix}. \tag{41}$$

To close the system we use the equation of state of a perfect gas

$$p = (\gamma - 1)\left(\rho E - \frac{1}{2}\rho(u^2 + v^2)\right). \tag{42}$$

We consider the smooth two-dimensional example of a convected isentropic vortex given for example by Hu and Shu [47]. The initial condition is a linear superposition of a homogeneous background field and some perturbations δ:

$$(\rho, u, v, p) = (1 + \delta\rho, 1 + \delta u, 1 + \delta v, 1 + \delta p). \tag{43}$$

The perturbations of the velocity components u and v as well as the perturbations of entropy $S = \frac{p}{\rho^\gamma}$ and temperature T of the vortex are given by

$$\begin{pmatrix} \delta u \\ \delta v \end{pmatrix} = \frac{\epsilon}{2\pi} e^{\frac{1-r^2}{2}} \begin{pmatrix} -(y-5) \\ (x-5) \end{pmatrix}, \quad \delta S = 0, \quad \delta T = -\frac{(\gamma-1)\epsilon^2}{8\gamma\pi^2} e^{1-r^2}, \tag{44}$$

with $r^2 = (x-5)^2 + (y-5)^2$, the vortex strength $\epsilon = 5$ and the ratio of specific heats $\gamma = 1.4$. If we define the relationship between density, pressure and static temperature in a non-dimensional fashion so that the gas constant becomes equal to unity, we obtain the following perturbations of the primitive variables density and pressure:

$$\delta\rho = (1 + \delta T)^{\frac{1}{\gamma-1}} - 1, \quad \delta p = (1 + \delta T)^{\frac{\gamma}{\gamma-1}} - 1. \tag{45}$$

The computational domain is $\Omega = [0; 10] \times [0; 10]$ and four periodic boundary conditions are imposed. After one period of $t = 10$, the exact solution is given by the initial condition (43). For measuring the error between the numerical solution u_p and the exact solution u_p^e, we first apply the reconstruction operator in order to get w_p from u_p and then we use the continuous L^2-norm

$$\|w_p - u_p^e\|_{L^2(\Omega)} = \left(\int_\Omega |w_h - u_e|^2 dV\right)^{\frac{1}{2}}, \tag{46}$$

in which the integration is approximated using Gaussian integration formulae with appropriate order of accuracy. We use the sequence of irregular triangular meshes shown in Fig. 5 (top) and set the Courant number to $0.7/(2N+1)$, except for the fifth- and sixth-order schemes where we use $0.5/(2N+1)$. The tolerance for the iterative solution of the nonlinear system arising from the local continuous space–time Galerkin method (24) via the iterative scheme (25) is set to 10^{-9} for the Euclidean norm of the vector $\Delta\widehat{\mathcal{U}}_{lp} = \widehat{\mathcal{U}}_{lp}^{1,i+1} - \widehat{\mathcal{U}}_{lp}^{1,i}$. This rather small tolerance is kept constant throughout the paper unless something else is explicitly specified.

The results obtained for all possible $P_N P_M$ schemes using the linear reconstruction operator as described in Section 2 are shown in Table 2 from second- to sixth-order of accuracy in space and time. Similar to the structure shown in Fig. 1 we present the pure finite volume schemes on the left of the table and the results obtained with pure DG schemes are reported on the diagonal, the intermediate $P_N P_M$ schemes are shown in between. The L^2 errors with the associated convergence rates for the density are presented. The first column of Table 2 entitled N_G characterizes the reciprocal mesh size and denotes the number of triangle edges used per space dimension. Note that there are two numbers given in this column, separated by a slash. The first number refers to the mesh size used for the finite volume schemes, the second number is valid for all the other $P_N P_M$ schemes. From Table 2 we conclude that for smooth problems high order finite volume schemes seem to be less accurate than the mixed $P_N P_M$ schemes and the pure DG schemes of the same accuracy on the same mesh. Furthermore, we observe that in this test case the $P_N P_M$ schemes with $N < M$ but N close to M are as accurate as the pure DG schemes, in particular on the finer meshes. For a quantitative efficiency comparison we also give the total CPU times in seconds in Table 3 as well as the total time in microseconds needed for all schemes to perform one entire time step per element (for all conserved variables), including reconstruction, iterative solution of the equations resulting from the local space–time Galerkin method and computation of the quadrature-free fluxes in the fully discrete schemes. The times given in Table 3 were measured on one CPU core

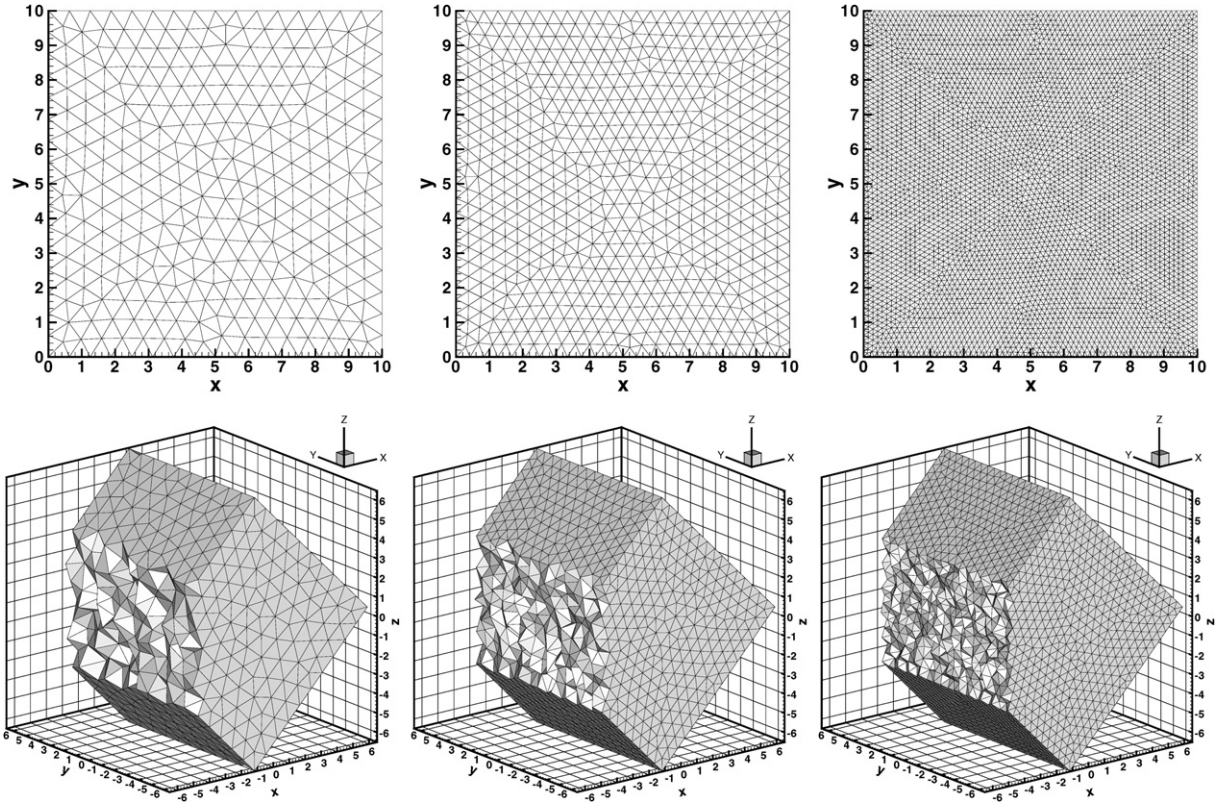

Fig. 5. Sequence of triangular meshes used for the two-dimensional convergence studies (top), and sequence of tetrahedral meshes used for the three-dimensional convergence studies (bottom).

Table 2
Two-dimensional $P_N P_M$ schemes from second- to sixth-order of accuracy applied to the Euler equations

N_G	L^2	$\mathcal{O}_{L^2}$	L^2	$\mathcal{O}_{L^2}$	L^2	$\mathcal{O}_{L^2}$	L^2	$\mathcal{O}_{L^2}$	L^2	$\mathcal{O}_{L^2}$	L^2	$\mathcal{O}_{L^2}$
$\mathcal{O}2$	P_0P_1		P_1P_1									
24/16	2.17E−01		5.56E−02									
32/24	1.27E−01	1.9	2.24E−02	2.2								
64/32	3.78E−02	1.7	9.75E−03	2.9								
128/64	9.97E−03	1.9	1.87E−03	2.4								
$\mathcal{O}3$	P_0P_2		P_1P_2		P_2P_2							
24/16	1.72E−01		3.17E−02		1.25E−02							
32/24	8.67E−02	2.4	7.11E−03	3.7	4.81E−03	2.3						
64/32	1.66E−02	2.4	2.10E−03	4.2	2.53E−03	2.2						
128/64	2.40E−03	2.8	1.35E−04	4.0	3.65E−04	2.8						
$\mathcal{O}4$	P_0P_3		P_1P_3		P_2P_3		P_3P_3					
24/16	4.45E−02		2.46E−02		3.37E−03		4.47E−03					
32/24	1.91E−02	2.9	3.86E−03	4.6	6.85E−04	3.9	8.86E−04	4.0				
64/32	1.41E−03	3.8	1.10E−03	4.4	1.96E−04	4.4	2.86E−04	3.9				
128/64	8.78E−05	4.0	4.06E−05	4.8	1.21E−05	4.0	1.90E−05	3.9				
$\mathcal{O}5$	P_0P_4		P_1P_4		P_2P_4		P_3P_4		P_4P_4			
24/16	3.54E−02		9.12E−03		1.20E−03		8.88E−04		8.78E−04			
32/24	1.58E−02	2.8	1.15E−03	5.1	1.65E−04	4.9	1.36E−04	4.6	1.46E−04	4.4		
64/32	8.31E−04	4.2	2.39E−04	5.5	4.31E−05	4.7	3.23E−05	5.0	3.93E−05	4.6		
128/64	3.14E−05	4.7	2.43E−06	6.6	2.75E−06	4.0	1.24E−06	4.7	1.56E−06	4.7		
$\mathcal{O}6$	P_0P_5		P_1P_5		P_2P_5		P_3P_5		P_4P_5		P_5P_5	
24/16	1.83E−02		7.67E−03		6.50E−04		2.28E−04		1.77E−04		2.11E−04	
32/24	3.56E−03	5.7	1.06E−03	4.9	5.98E−05	5.9	2.07E−05	5.9	1.63E−05	5.9	1.94E−05	5.9
64/32	1.08E−04	5.0	1.83E−04	6.1	1.08E−05	5.9	3.69E−06	6.0	2.82E−06	6.1	3.26E−06	6.2
128/48	1.49E−06	6.2	1.13E−05	6.9	1.48E−06	4.9	3.43E−07	5.9	2.63E−07	5.8	3.08E−07	5.8

Errors for density ρ are shown.

of an Intel Core 2 Duo computer with 2 GHz clock speed and 2 GB of RAM. We also give the CPU time needed for one element update (EU), which is computed by dividing the total CPU time by the number of time steps and the number of elements in the mesh. To be able to compare the CPU times between 2D and 3D computations as well as to allow a comparison with different hyperbolic systems, we also give the CPU time per degree of freedom update (DU), which is the time per element update divided by the number of equations in the hyperbolic system and the number of degrees of freedom in the scheme used to represent the data, i.e. L_N. We give this additional information to allow for a direct efficiency comparison with other methods, such as e.g. high order finite difference schemes. Based on these CPU times we conclude that in 2D the new class of intermediate $P_N P_M$ schemes is much more efficient than pure finite volume or pure DG schemes.

Example: in order to reach an error of about 3×10^{-5} the pure fifth-order DG scheme (P_4P_4) needs approximately 900 s. On the same 32^2 mesh the new P_3P_4 method reaches the same error in only about 450 s and the P_2P_4 method even needs only about 300 s to reach this level of accuracy. For comparison, the computation with the fifth-order finite volume method (P_0P_4) takes about 2800 s on a 128^2 mesh to reach an error or 3×10^{-5}.

5.2.2. Three-dimensional ideal MHD equations

In this section we consider a more complicated hyperbolic system than the Euler equations used in the previous two-dimensional case. We solve the equations of ideal magnetohydrodynamics (MHD) in three space dimensions. The MHD system introduces an additional difficulty for numerical schemes since the divergence of the magnetic field must remain zero in time, i.e.

$$\frac{\partial B_x}{\partial x} + \frac{\partial B_y}{\partial y} + \frac{\partial B_z}{\partial z} = 0, \tag{47}$$

Table 3
Total CPU times in seconds associated to the results presented in Table 2 and (in bold letters) time in microseconds needed by the schemes to perform one entire element update (EU) and one single degree of freedom update (DU) for the 2D Euler equations

N_G						
$\mathcal{O}2$	P_0P_1	P_1P_1				
24/16	2.2	2.3				
32/24	5.4	7.5				
64/32	44.0	17.9				
128/64	408	145				
μs/EU	**7.5**	**8.3**				
μs/DU	**1.9**	**0.7**				
$\mathcal{O}3$	P_0P_2	P_1P_2	P_2P_2			
24/16	3.8	4.2	8.2			
32/24	9.2	14.0	27.0			
64/32	73.8	33.8	65.0			
128/64	681	272	524			
μs/EU	**13**	**16**	**18**			
μs/DU	**3.1**	**1.3**	**0.8**			
$\mathcal{O}4$	P_0P_3	P_1P_3	P_2P_3	P_3P_3		
24/16	8.1	8.4	16.8	27.3		
32/24	19.5	28.4	56.6	91.6		
64/32	151	68.1	136	221		
128/64	1352	539	1077	1758		
μs/EU	**25**	**31**	**37**	**43**		
μs/DU	**6.2**	**2.6**	**1.5**	**1.1**		
$\mathcal{O}5$	P_0P_4	P_1P_4	P_2P_4	P_3P_4	P_4P_4	
24/16	19.3	19.5	35.9	58.4	120	
32/24	45.0	64.2	119	192	392	
64/32	332	151	280	450	925	
128/64	2829	1145	2126	3480	7193	
μs/EU	**52**	**65**	**73**	**85**	**98**	
μs/DU	**10**	**5.5**	**3.0**	**2.1**	**1.6**	
$\mathcal{O}6$	P_0P_5	P_1P_5	P_2P_5	P_3P_5	P_4P_5	P_5P_5
24/16	45.3	46.2	80.0	118	232	321
32/24	101	144	249	378	747	1034
64/32	688	327	573	876	1754	2466
128/48	8573	1381	2469	3840	7768	10,818
μs/EU	**140**	**140**	**150**	**160**	**180**	**210**
μs/DU	**34**	**11**	**6.1**	**4.1**	**3.1**	**2.5**

which for the analytical problem is always satisfied under the condition that the initial data of $\vec{B}$ are divergence-free. From the discrete point of view this is not necessarily guaranteed and hence extra care is required in the discretization. In this article we use the hyperbolic version of the generalized Lagrangian multiplier (GLM) divergence cleaning approach proposed in [23]. It consists in adding an auxiliary variable Ψ and one linear scalar PDE to the MHD system to transport divergence errors out of the computational domain with the artificial speed c_h. This is quite similar as role of the pressure in the incompressible Navier–Stokes equations. The augmented MHD system with hyperbolic GLM divergence cleaning has the state vector $u_p = (\rho, \rho v_j, \rho E, B_j, \Psi)^{\mathrm{T}}$ and the following flux tensor:

$$\vec{F}_p = F_{pi} = \begin{pmatrix} \rho v_i \\ \rho v_i v_j + \left(p + \frac{1}{8\pi}\vec{B}^2\right)\delta_{ij} - \frac{1}{4\pi}B_iB_j \\ v_i\left(\rho E + p + \frac{1}{8\pi}\vec{B}^2\right) - \frac{1}{4\pi}B_i(v_kB_k) \\ v_iB_j - B_iv_j + \Psi\delta_{ij}, \\ c_h^2 B_i \end{pmatrix} \tag{48}$$

with the velocity vector $\vec{v} = v_i = (u, v, w)^{\mathrm{T}}$ and the magnetic field vector $\vec{B} = B_i = (B_x, B_y, B_z)^{\mathrm{T}}$. The equation of state is

$$p = (\gamma - 1)\left(\rho E - \frac{1}{2}\vec{v}^2 - \frac{\vec{B}^2}{8\pi}\right). \tag{49}$$

For the numerical convergence studies in 3D of the proposed quadrature-free $P_N P_M$ schemes, we solve a 3D version of the 2D vortex test problem proposed by Balsara [4]. The fully three-dimensional version of the problem is obtained by rotating the 3D domain $\Omega\prime = [-5; 5]^3$ by 45° around the y-axis. Six periodic boundary conditions are imposed. The unstructured tetrahedral mesh sequence used for this test as well as the rotated final computational domain Ω are seen in Fig. 5 (bottom). The initial condition using the vector of primitive variables, $W_p = (\rho, u, v, w, p, B_x, B_y, B_z, \Psi)^{\mathrm{T}}$, is

$$W_p = \left(1, \frac{\sqrt{2}}{2} + \delta u, 1 + \delta v, \frac{\sqrt{2}}{2} + \delta w, 1 + \delta p, \delta B_x, \delta B_y, \delta B_z, 0\right)^{\mathrm{T}} \tag{50}$$

with the following relations for the perturbations, using $\delta\vec{v} = (\delta u, \delta v, \delta w)^{\mathrm{T}}$ and $\delta\vec{B} = (\delta B_x, \delta B_y, \delta B_z)^{\mathrm{T}}$:

$$\vec{\lambda} = \frac{1}{2}\sqrt{2}(1, 0, 1)^{\mathrm{T}}, \quad \vec{r} = (1 - \vec{x}\cdot\vec{\lambda})\vec{x}, \quad r = \|\vec{r}\|,$$
$$\delta\vec{v} = \frac{\kappa}{2\pi} e^{q(1-r^2)}\vec{\lambda}\times\vec{r}, \quad \delta\vec{B} = \frac{\mu}{2\pi}\mathrm{e}^{q(1-r^2)}\ \vec{\lambda}\times\vec{r}, \tag{51}$$
$$\delta p = \frac{1}{64q\pi^3}(\mu^2(1 - 2qr^2) - 4\kappa^2\pi)\mathrm{e}^{2q(1-r^2)}. \tag{52}$$

The speed for the divergence cleaning is set to $c_h = 3$ in the whole domain and the parameters κ and μ are set to $\kappa = 1$ and $\mu = \sqrt{4\pi}$ according to [4]. After one period at time $t = 10$ the exact solution is given by the initial condition. Compared to the test case proposed by Balsara [4] we introduce an additional parameter q in Eq. (51) and (52), which plays a very important role in this test case when using very high order schemes. In [4], the smallest error norm of the magnetic field obtained with the best second-order scheme on the finest mesh (800×800 elements) was of the order 10^{-5}. This is precisely the order of magnitude of the perturbation $\delta\vec{B}$ at the radial boundaries of the computational domain, since the exponential function is never exactly zero, but will always produce some small contributions. Since B_y and B_x have opposite signs on the left and right and on the top and bottom boundary of Ω, respectively, there is a jump in the magnetic field at the boundaries due to the periodic boundary conditions. In the numerical convergence studies these discontinuities cause first-order disturbances of the order 10^{-5} and for sufficiently high order accurate schemes on sufficiently fine meshes, the small jump at the boundary will lead to dominant first-order errors. We therefore decide to use the value $q = \frac{1}{2}$ according to [4] only for schemes up to fourth-order of accuracy, since the smallest error obtained on the finest mesh is still larger than 10^{-5}. For the fifth- and sixth-order accurate schemes, which are very accurate even on the coarse meshes used in this paper, we decide to use $q = 1$. This leads to a more difficult test case due to a narrower Gaussian function, but resulting in jumps in the magnetic field of only 10^{-10} at the boundaries, thus guaranteeing that the small discontinuities at the boundaries will not deteriorate our convergence results. The iso-surfaces of pressure, u- and v-velocity components as well as several magnetic streamlines are depicted in Fig. 6 on an unstructured 40^3 mesh after one full advection period at $t = 10$ using the P_3P_4 scheme. With the notation N_G^3 for unstructured tetrahedral meshes we denote the number of tetrahedron edges N_G per space dimension. The total number of elements inside such a N_G^3 mesh is then roughly between $6N_G^3$ and $7N_G^3$ since the volume of the unit tetrahedron is only $1/6$. The numerical solution obtained with the P_3P_4 scheme after one advection period is practically identical to the initial condition, as confirmed by the convergence rates and error norms given for the velocity component w and the magnetic field component B_x shown for this three-dimensional test case in Tables 4 and 5.

The detailed CPU times (wallclock times) associated with our computations done on 64 CPUs of the HLRB2 supercomputer of the *Leibniz Rechenzentrum* in München, Germany, are given in Table 6. The CPU times per element update (wallclock time × number of CPU/number of elements/number of time steps) already include all the necessary MPI communications on the supercomputer. From the convergence results

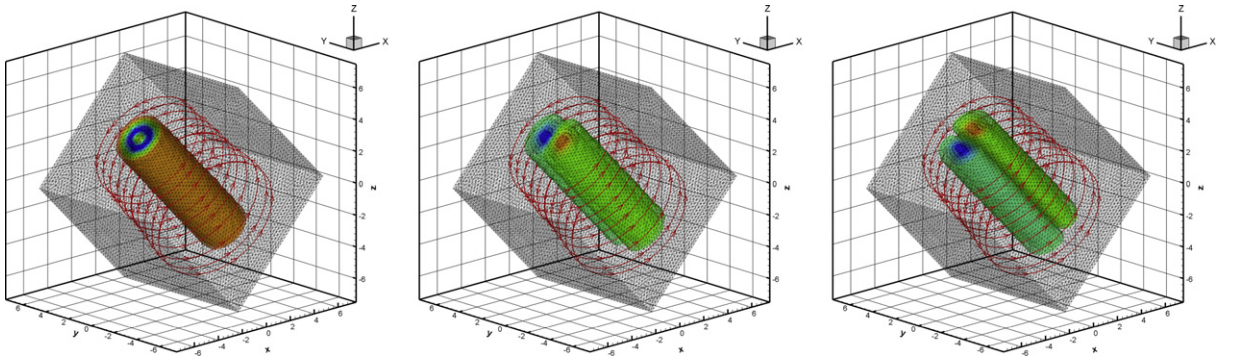

Fig. 6. Iso-surfaces for p, u and v (from left to right) and streamlines for the magnetic field $\vec{B}$ after one full advection period at $t = 10$ using a P_3P_4 scheme on a 40^3 mesh containing 434,327 tetrahedrons.

Table 4
Three-dimensional P_NP_M schemes from second- to sixth-order of accuracy applied to the ideal MHD equations

N_G	L^2	$\mathcal{O}_{L^2}$	L^2	$\mathcal{O}_{L^2}$	L^2	$\mathcal{O}_{L^2}$	L^2	$\mathcal{O}_{L^2}$	L^2	$\mathcal{O}_{L^2}$
$\mathcal{O}2$	P_1P_1									
10	1.90E−01									
20	4.39E−02	2.1								
30	1.60E−02	2.5								
40	6.81E−03	3.0								
$\mathcal{O}3$	P_1P_2		P_2P_2							
10	7.97E−02		1.68E−02							
20	7.46E−03	3.4	2.44E−03	2.8						
30	1.75E−03	3.6	8.11E−04	2.7						
40	5.75E−04	3.9	3.18E−04	3.3						
$\mathcal{O}4$	P_1P_3		P_2P_3		P_3P_3					
10	5.20E−02		4.91E−03		2.20E−03					
20	3.27E−03	4.0	4.03E−04	3.6	1.97E−04	3.5				
30	5.40E−04	4.4	9.48E−05	3.6	4.70E−05	3.5				
40	1.20E−04	5.2	2.75E−05	4.3	1.42E−05	4.2				
$\mathcal{O}5$	P_1P_4		P_2P_4		P_3P_4		P_4P_4			
10	7.82E−02		1.04E−02		4.83E−03		1.60E−03			
20	3.68E−03	4.4	3.92E−04	4.7	2.26E−04	4.4	1.31E−04	3.6		
30	3.65E−04	5.7	6.08E−05	4.6	3.87E−05	4.4	2.54E−05	4.0		
40	5.12E−05	6.8	1.30E−05	5.4	8.52E−06	5.3	6.27E−06	4.9		
$\mathcal{O}6$	P_1P_5		P_2P_5		P_3P_5		P_4P_5		P_5P_5	
10	6.71E−02		6.89E−03		1.78E−03		8.09E−04		5.75E−04	
15	1.37E−02	3.9	7.94E−04	5.3	2.63E−04	4.7	1.62E−04	4.0	1.34E−04	3.6
20	2.46E−03	6.0	1.21E−04	6.5	5.50E−05	5.4	3.60E−05	5.2	3.32E−05	4.9
30	1.96E−04	6.2	1.19E−05	5.7	6.35E−06	5.3	3.78E−06	5.6	4.36E−06	5.0

Errors for velocity field component w are shown.

for the velocity component w (Table 4) and the CPU times (Table 6) we clearly deduce again that the new intermediate class of schemes is superior in efficiency compared to the standard DG method. This result holds also for all the other classical Euler flow quantities ρ, u, v and p. However, for the magnetic field components B_x, B_y and B_z, the pure DG scheme is computationally the most efficient. Further work will be needed to devise essentially divergence-free P_NP_M reconstruction operators on unstructured meshes, following the ideas given for second-order TVD schemes in [4].

Table 5
Three-dimensional $P_N P_M$ schemes from second- to sixth-order of accuracy applied to the ideal MHD equations

N_G	L^2	$\mathcal{O}_{L^2}$	L^2	$\mathcal{O}_{L^2}$	L^2	$\mathcal{O}_{L^2}$	L^2	$\mathcal{O}_{L^2}$	L^2	$\mathcal{O}_{L^2}$
$\mathcal{O}2$	P_1P_1									
10	7.54E−01									
20	1.83E−01	2.0								
30	6.71E−02	2.5								
40	2.81E−02	3.0								
$\mathcal{O}3$	P_1P_2		P_2P_2							
10	3.07E−01		6.26E−02							
20	2.88E−02	3.4	8.30E−03	2.9						
30	6.54E−03	3.7	2.64E−03	2.8						
40	2.03E−03	4.1	1.02E−03	3.3						
$\mathcal{O}4$	P_1P_3		P_2P_3		P_3P_3					
10	1.51E−01		1.80E−02		7.15E−03					
20	1.10E−02	3.8	1.34E−03	3.7	5.65E−04	3.7				
30	2.32E−03	3.8	3.11E−04	3.6	1.31E−04	3.6				
40	7.34E−04	4.0	8.75E−05	4.4	3.95E−05	4.2				
$\mathcal{O}5$	P_1P_4		P_2P_4		P_3P_4		P_4P_4			
10	2.89E−01		4.03E−02		1.67E−02		3.96E−03			
20	1.38E−02	4.4	1.36E−03	4.9	6.90E−04	4.6	2.38E−04	4.1		
30	1.34E−03	5.8	2.00E−04	4.7	1.07E−04	4.6	3.78E−05	4.5		
40	1.84E−04	6.9	4.12E−05	5.5	2.20E−05	5.5	8.07E−06	5.4		
$\mathcal{O}6$	P_1P_5		P_2P_5		P_3P_5		P_4P_5		P_5P_5	
10	2.48E−01		2.71E−02		6.00E−03		2.32E−03		8.81E−04	
15	5.13E−02	3.9	2.99E−03	5.4	8.31E−04	4.9	3.92E−04	4.4	1.59E−04	4.2
20	9.30E−03	5.9	4.31E−04	6.7	1.68E−04	5.6	7.50E−05	5.7	3.13E−05	5.7
30	7.42E−04	6.2	3.93E−05	5.9	1.77E−05	5.5	1.33E−05	4.3	3.43E−06	5.5

Errors for magnetic field component B_x are shown.

Thanks to the use of our very high order accurate schemes, the error norms decrease quickly even on very coarse meshes using at most 40 elements per space dimension. We remind the reader that the best error norms obtained in [4] with second-order TVD schemes were of the order 10^{-5} on 800×800 meshes for $q = \frac{1}{2}$, corresponding to an equivalent total number of 512×10^6 grid points for a fully 3D computation as presented here. The proposed P_3P_4 scheme reaches this accuracy for the even more difficult test case with $q = 1$ and only needs 8.68654×10^6 degrees of freedom per variable on the finest mesh with 434,327 tetrahedrons. The number of spatial degrees of freedom of a $P_N P_M$ scheme and the number of mesh points for a second-order TVD finite volume scheme can be directly compared to each other and show the drastic benefits for memory storage efficiency using very high order accurate methods compared to standard second-order TVD schemes.

We must emphasize that we did *not* obtain the correct convergence rates *without* the use of the divergence cleaning approach. Although the error norms were small even without divergence cleaning, the full formal order of accuracy could not be observed. This is a strong indication that high order schemes *alone* are *not* able to resolve the problem of the divergence-free condition of the magnetic field for MHD computations on unstructured meshes in multiple space dimensions.

6. Applications

To validate the new one-step time integration approach, obtained by the local space–time continuous Galerkin formulation introduced in Section 3 of this paper, on problems with discontinuous solutions, we solve a broad spectrum of different challenging hyperbolic systems on unstructured meshes in two and three space dimensions. Therefore, the ideal and relativistic MHD equations as well as the equations of nonlinear elasticity are tackled. Since we want to show the capability of the continuous space–time Galerkin predictor method also in the presence of shock waves and other discontinuities, we now restrict ourselves to the pure

Table 6
Total CPU times in seconds associated to the results presented in Tables 4 and 5 and (in bold letters) time in microseconds needed by the schemes to perform one entire element update (EU)and one single degree of freedom update (DU) for the 3D ideal MHD equations

N_G					
$\mathcal{O}2$	P_1P_1				
10	23.6				
20	169				
30	705				
40	2466				
μs/EU	**51**				
μs/DU	**1.42**				
$\mathcal{O}3$	P_1P_2	P_2P_2			
10	37	71			
20	297	590			
30	1382	2653			
40	4797	25,731			
μs/EU	**99**	**113**			
μs/DU	**3.8**	**1.2**			
$\mathcal{O}4$	P_1P_3	P_2P_3	P_3P_3		
10	88	163	256		
20	747	1453	2271		
30	3422	6611	10,541		
40	11,641	22,750	35,833		
μs/EU	**216**	**253**	**285**		
μs/DU	**6.0**	**2.8**	**1.5**		
$\mathcal{O}5$	P_1P_4	P_2P_4	P_3P_4	P_4P_4	
10	205	364	561	987	
20	1718	3131	4943	8700	
30	7719	13,828	21,737	38,696	
40	25,823	46,394	72,458	132,470	
μs/EU	**533**	**575**	**641**	**729**	
μs/DU	**15**	**6.4**	**3.6**	**2.3**	
$\mathcal{O}6$	P_1P_5	P_2P_5	P_3P_5	P_4P_5	P_5P_5
10	591	982	1744	2439	3303
15	1905	3160	5963	8418	11,315
20	4543	7908	14,849	20,761	28,298
30	20,109	34,681	64,517	94,317	125,713
μs/EU	**1510**	**1563**	**1662**	**1890**	**2061**
μs/DU	**42**	**17**	**9.23**	**6.0**	**4.1**

finite volume case P_0P_M in all those test cases with discontinuities, where we use the nonlinear WENO reconstruction operator on unstructured meshes proposed in [28] and [29], since the nonlinear version of the general P_NP_M reconstruction operator will be the subject of future work. We use the following parameters for the WENO scheme [29]: $\lambda_1 = 10^5$, $r = 8$ and $\epsilon = 10^{-14}$.

6.1. Ideal MHD equations

6.1.1. 3D MHD shock tube problems

The first test case is a set of three Riemann problems, solved on a fully unstructured tetrahedral mesh (see Fig. 7) consisting of 186,145 elements with characteristic mesh length $h = \frac{1}{400}$. The computational domain is $\Omega = [-0.5; 0.5] \times [-0.01; 0.01]^2$ with periodic boundary conditions in y and z directions and transmissive boundaries in x-direction. In our fully three-dimensional computations we use the P_0P_2 scheme with characteristic WENO reconstruction. The initial condition consists of two piecewise constant states (see Table 7), separated by a discontinuity at $x = 0$.

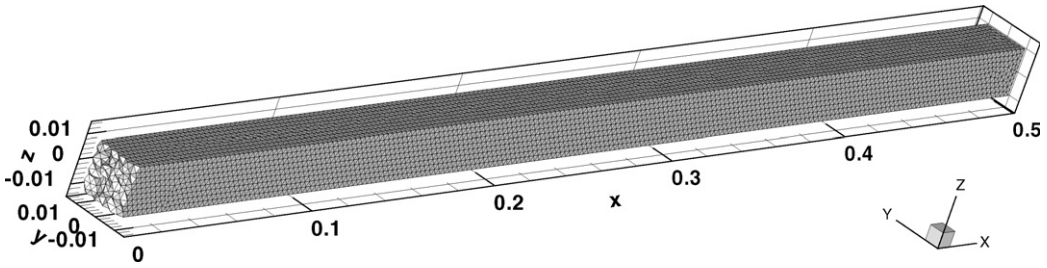

Fig. 7. The mesh for the 3D shock tube problems. Only the part $x > 0$ is shown.

Table 7
Initial states left (L) and right (R) for the 3D shock tube problems for the ideal MHD equations in 3D

	ρ	u	v	w	p	B_x	B_y	B_z
Case 1 (Lax problem): $\gamma = 1.4,\ c_h = 0,\ t_e = 0.14$								
L	0.445	0.698	0.0	0.0	3.528	0.0	0.0	0.0
R	0.5	0.0	0.0	0.0	0.571	0.0	0.0	0.0
Case 2 (Brio and Wu problem): $\gamma = 2.0,\ c_h = 2,\ t_e = 0.10$								
L	1.0	0.0	0.0	0.0	1.0	$0.75\sqrt{4\pi}$	$\sqrt{4\pi}$	0.0
R	0.125	0.0	0.0	0.0	0.1	$0.75\sqrt{4\pi}$	$\sqrt{4\pi}$	0.0
Case 3 (Ryu and Jones problem): $\gamma = \frac{5}{3},\ c_h = 2,\ t_e = 0.20$								
3L	1.08	1.2	0.01	0.5	0.95	2.0	3.6	2.0
3R	0.9891	−0.0131	0.0269	0.010037	0.97159	2.0	4.0244	2.0026

Values for γ, c_h and t_e are also given.

The first test case is the classical Lax shock tube problem [51] for the Euler equations of compressible gas dynamics. In our present test case, we solve the full MHD system (48), but with the magnetic fields switched off. The exact reference solution is then given by the exact solution of the classical Riemann problem for the Euler equations. The other two test cases correspond to the shock tube problems proposed by Brio and Wu [11] and Ryu and Jones [63], for which an exact solution is available. For test case 2 we compute a numerical reference solution in 1D using a second-order TVD finite volume scheme on 20,000 elements. In Fig. 8 we show, for each test case, cuts through the domain Ω along the x-axis using 400 equidistant sample points. In all cases, we obtain an excellent agreement between the numerical solution, obtained on the 3D tetrahedral mesh, and the 1D reference solutions.

6.1.2. MHD rotor problem

The second test case is the well-known MHD rotor problem proposed by Balsara and Spicer in [7]. It consists of a rapidly rotating fluid of high density embedded in a fluid at rest with low density. Both fluids are subject to an initially constant magnetic field. The rotor causes torsional Alfvén waves to be launched into the fluid at rest. As a result the angular momentum of the rotor is diminished. The problem is set up on a circular computational domain Ω with radius $r = \frac{1}{2}$ using a locally refined mesh towards the center of the domain with a total number of 106,842 triangles. The characteristic mesh size is $h = 0.003$ for $0 \leqslant r \leqslant 0.13$ and $h = 0.005$ for $0.13 < r \leqslant 0.5$. The density of the rotor is $\rho = 10$ for $0 \leqslant r \leqslant 0.1$ and $\rho = 1$ for the ambient fluid. The rotor has a constant angular velocity ω that is determined in such a way to obtain a toroidal velocity of $v = \omega \cdot r = 1$ at $r = 0.1$. The pressure is $p = 1$ in the whole domain and the magnetic field vector is set to $\vec{B} = (2.5, 0, 0)^{\mathrm{T}}$ in the whole domain. As proposed by Balsara and Spicer we apply a linear taper to the velocity and density field in the range from $0.1 \leqslant r \leqslant 0.13$ such that density and velocity match those of the ambient fluid at rest at a radius of $r = 0.13$. The speed for the hyperbolic divergence cleaning is set to $c_h = 2$ and $\gamma = 1.4$ is used. Transmissive boundary conditions are applied at the outer boundaries. A zoom into the computational domain together with the triangular mesh and a contour plot of the magnetic pressure at time

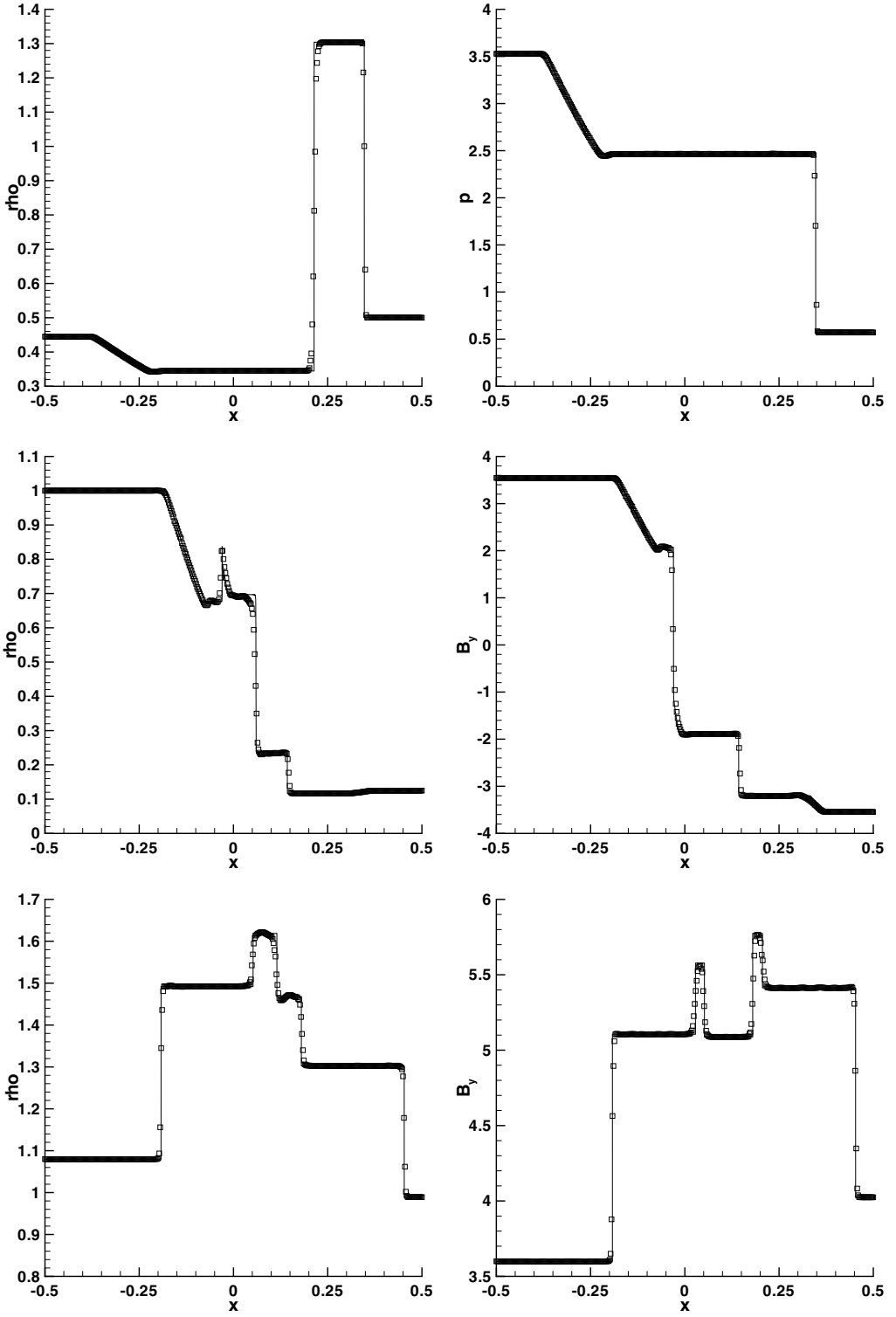

Fig. 8. Results for the 3D MHD shock tube problems (test cases 1–3 from top to bottom). P_0P_2 scheme with characteristic WENO reconstruction on unstructured tetrahedral mesh (squares) and reference solution (solid line).

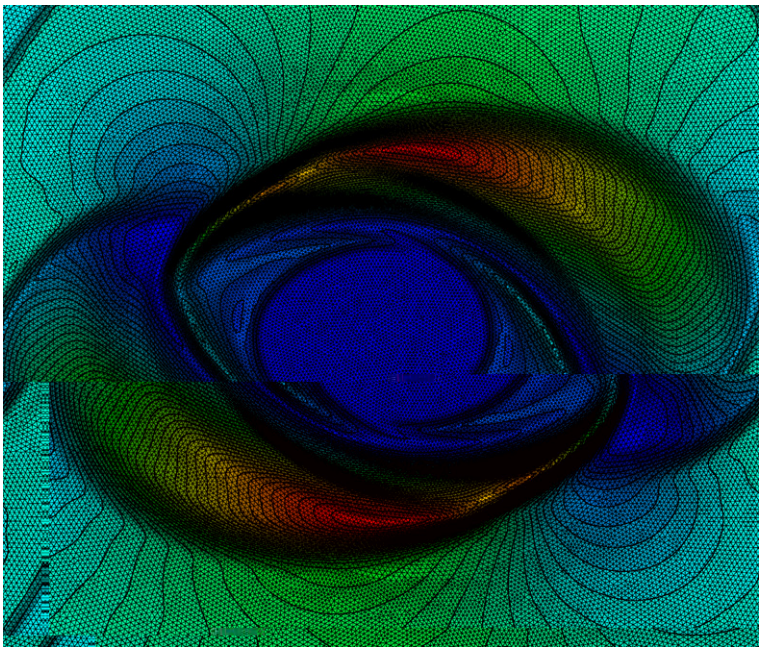

Fig. 9. Zoom into the triangular mesh used for the MHD rotor problem together with a contour plot of the magnetic pressure at $t = 0.25$.

$t = 0.25$ is given in Fig. 9. The whole domain together with the results for density, pressure, Mach number and magnetic pressure obtained after 745 time steps at $t = 0.25$ are depicted in detail in Fig. 10. Compared to the results presented by Balsara and Spicer we note a very good agreement. We emphasize that thanks to the divergence cleaning, no spurious oscillations can be seen in the density field and in the magnetic pressure, as reported by Balsara and Spicer for Godunov schemes without divergence cleaning. We used a P_0P_2 scheme with simple *componentwise* WENO reconstruction. The total CPU time was 76 min on one single CPU core of an Intel Core 2 Duo computer with 2GHz clockspeed and 2 GB of RAM. From this information we can deduce the total time needed for one element update being 57 μs. This CPU time needed for the nine equations of the augmented GLM-MHD system together with a nonlinear WENO reconstruction compares very well to the results obtained for the linear P_0P_2 scheme in the section on convergence studies for the four equations of the 2D Euler system (13 μs).

6.1.3. Orszag–Tang vortex system

The last test case that we consider for the ideal MHD equations is the vortex system of Orszag and Tang [55] which was studied extensively in [56] and [22]. The computational domain is $\Omega = [0; 2\pi]^2$. We use the parameters of the computation of Jiang and Wu [48], scaling the magnetic field by $\sqrt{4\pi}$ due to the different normalization of the governing equations. The initial condition of the problem is given by

$$(\rho, u, v, p, B_x, B_y) = \left(\gamma^2, -\sin(y), \sin(x), \gamma, -\sqrt{4\pi}\sin(y), \sqrt{4\pi}\sin(2x)\right) \tag{53}$$

with $w = B_z = 0$ and $\gamma = \frac{5}{3}$. The problem is solved up to $t = 5.0$ using a P_0P_2 scheme with componentwise WENO reconstruction on an unstructured triangular mesh with 89,832 elements ($h = \frac{1}{200}$). The divergence cleaning speed is set to $c_h = 2.0$. The results for pressure are shown in Fig. 11 for $t = 0.5$, $t = 2.0$, $t = 3.0$ and $t = 5.0$, showing an excellent agreement with the fifth-order WENO finite difference solution computed by Jiang and Wu [48] on a 192^2 Cartesian grid. The computation for 1533 time steps until $t = 5.0$ took 131 min on one CPU core of a 2 GHz Intel Core 2 Dual Core computer with 2 GB of RAM, leading again to 57 μs per element update.

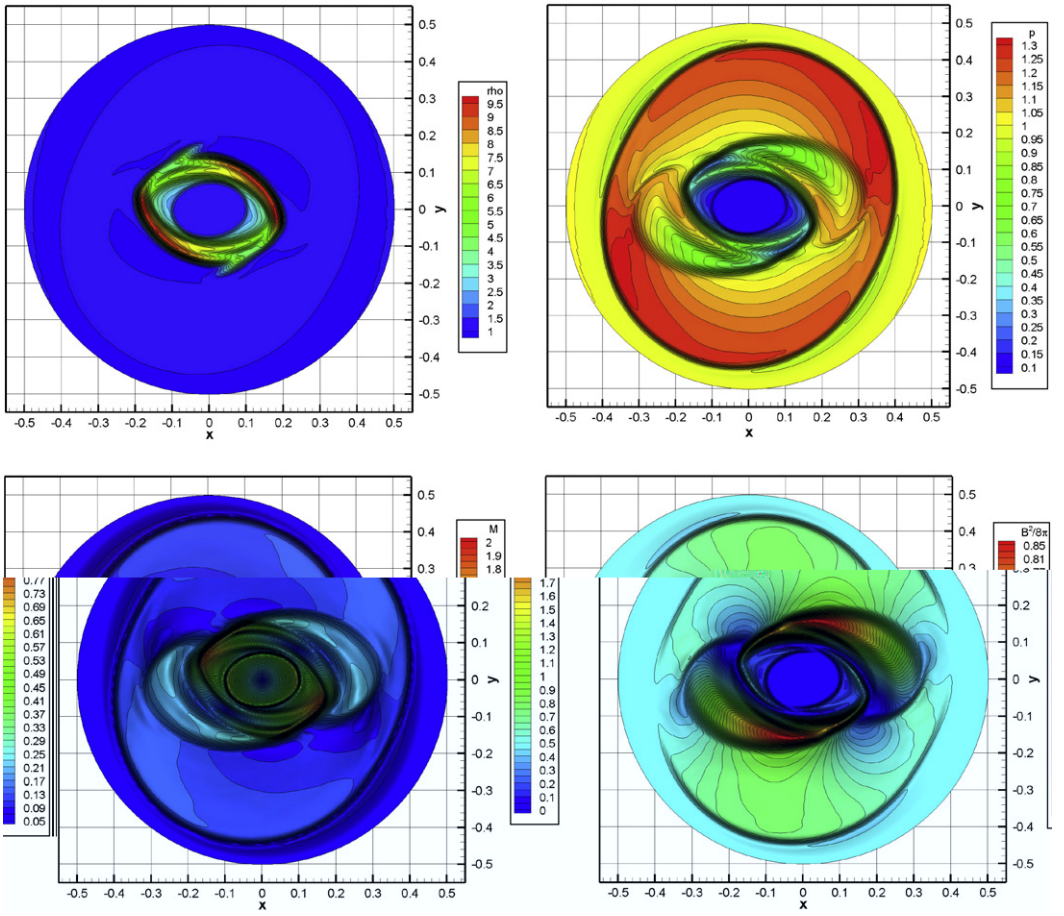

Fig. 10. Results for density, pressure, Mach number and magnetic pressure, obtained for the MHD rotor problem at $t = 0.25$ using the P_0P_2 scheme with componentwise WENO reconstruction.

6.2. Relativistic MHD equations

The relativistic MHD (RMHD) equations form a very complicated hyperbolic system, for which an analytic or even semi-analytic version of the Cauchy–Kovalewski (Lax–Wendroff) procedure as proposed in [34,32,68,29] becomes impossible for orders greater than two. This limitation is due to the fact that the primitive variables that enter the physical flux cannot be expressed any more in a closed analytical form in terms of the conserved quantities. The local space–time continuous Galerkin scheme proposed in this paper for local data evolution in time is very general, since it is only based on flux and source evaluations at the local space–time nodes, and is therefore suitable to build a one-step scheme of order larger than two even for the relativistic MHD equations. The details about this very interesting hyperbolic system can be found in [3,82,38,46,61]. For the multidimensional version of the equations, we also have to enforce the divergence-free condition of the magnetic field as in the non-relativistic MHD case. This is done again using the hyperbolic divergence-cleaning approach proposed by Dedner et al. [23]. Using the notation of [82] the vector of conserved variables is given in terms of the primitive variables ρ, v_j, p, B_j and Ψ by

$$u_p = \begin{pmatrix} D \\ Q_j \\ E \\ B_j \\ \Psi \end{pmatrix} = \begin{pmatrix} \gamma\rho \\ \gamma w_{\mathrm{tot}} v_j - b^0 b^j \\ \gamma^2 w_{\mathrm{tot}} - b^0 b^0 - p_{\mathrm{tot}} \\ B_j \\ \Psi \end{pmatrix}. \tag{54}$$

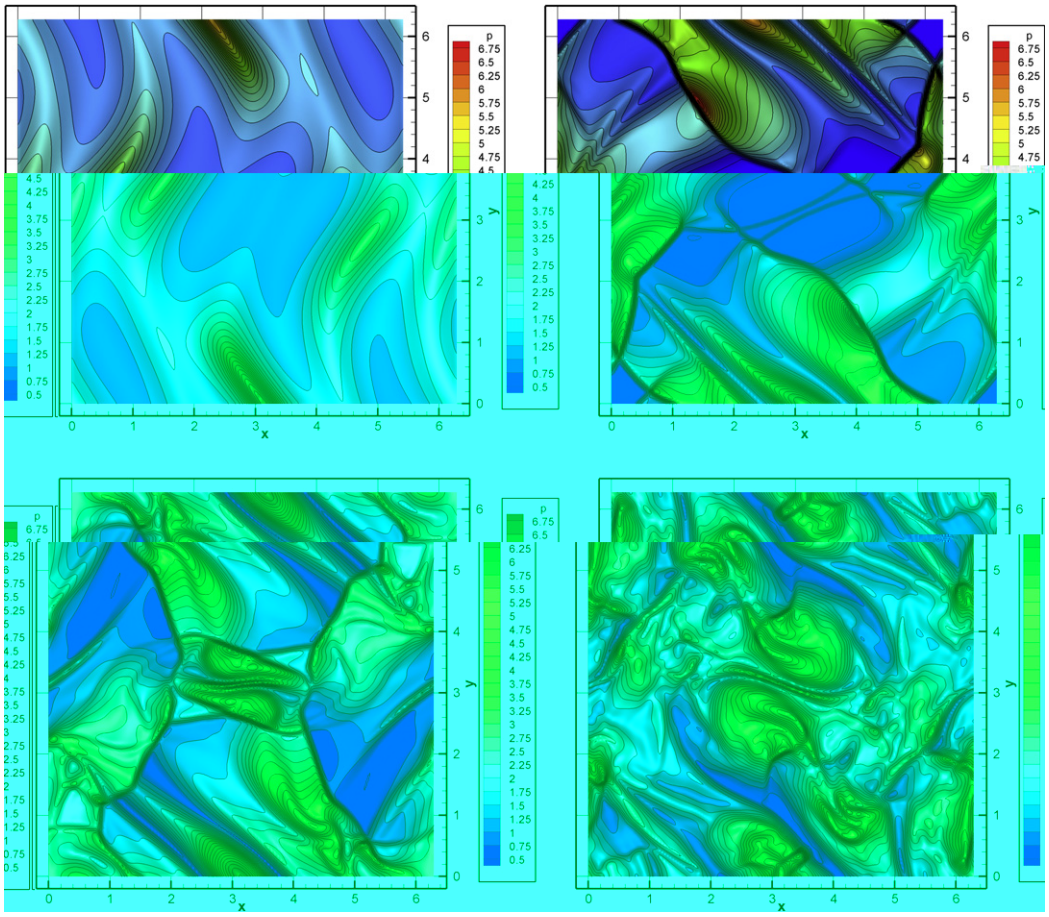

Fig. 11. Evolution of the pressure field of the Orszag–Tang problem at times $t = 0.5$, $t = 2.0$, $t = 3.0$ and $t = 5.0$ (top left to bottom right) using the P_0P_2 scheme with componentwise WENO reconstruction.

The flux tensor is defined in multiple space dimensions as

$$\vec{F}_p = F_{pi} = \begin{pmatrix} \gamma \rho v_i, \\ \gamma^2 w_{\mathrm{tot}} v_i v_j - b^i b^j + p_{\mathrm{tot}} \delta_{ij}, \\ \gamma^2 w_{\mathrm{tot}} v_i - b^0 b^i \\ v_i B_j - B_i v_j + \Psi \delta_{ij} \\ c_h^2 B_i \end{pmatrix}. \tag{55}$$

The equation of state is

$$e = \rho + \frac{p}{\Gamma - 1}, \tag{56}$$

the Lorentz factor, denoted as γ in this section, is defined by

$$\gamma = \frac{1}{\sqrt{1 - \vec{v}^2}}, \tag{57}$$

further quantities appearing in (54) and (55) are given by

$$b^0 = \gamma v_k B_k, \;\; b^i = \frac{B_i}{\gamma} + \gamma v_i (v_k B_k), \quad |b|^2 = \frac{\vec{B}^2}{\gamma^2} + (v_k B_k)^2 \tag{58}$$

from which total enthalpy and total pressure are then finally defined as

$$w_{\text{tot}} = e + p + |b|^2, \qquad p_{\text{tot}} = p + \frac{1}{2}|b|^2. \tag{59}$$

In this entire section, the speed of light is supposed to be set to unity. The computation of the primitive variables ρ, v_k and p from the vector u_p of conserved quantities is very complicated. It can not be done analytically but requires necessarily the use of an iterative technique such as Newton's method. A very elegant, robust and efficient way of transforming the conservative variables to primitive variables using the analytic inversion of a third degree polynomial together with one nonlinear scalar equation to which subsequently Newton's method is applied is given in [82]. For the reader who may not be familiar with the procedure described in [82], we give a very brief summary here. For the primitive variables, the following relations hold according to [82],

$$\rho = D\sqrt{1-\vec{v}^2}, \quad p = ((1-\vec{v}^2)W - \rho)/\Gamma, \quad v_j = \frac{1}{W+\vec{B}^2}\left(Q_j + \frac{S}{W}B_j\right), \tag{60}$$

with $S = Q_k B_k = W v_k B_k$ and the auxiliary variable W. Introducing $T^2 = \vec{B}^2\vec{Q}^2 - S^2$ and algebraic manipulations yield the following cubic equation for the auxiliary variable W in terms of the unknown $\vec{v}^2$:

$$\left[\left(1 - \frac{1-\vec{v}^2}{\Gamma}W - E + \frac{\rho}{\Gamma} + \frac{\vec{B}^2}{2}\right)\right](W+\vec{B}^2)^2 + \frac{T^2}{2} = 0. \tag{61}$$

This cubic equation can be solved analytically for $W = W(\vec{v}^2)$ for a given $\vec{v}^2$ and it is shown in [82] that all solutions of (61) are real and that always the largest solution is the physically correct one. The unknown $\vec{v}^2$ can then be computed numerically via Newton's method according to [82] from the nonlinear equation,

$$\mathbb{F}(\vec{v}^2) = (W(\vec{v}^2))^2\vec{v}^2 + T^2\frac{2W(\vec{v}^2)+\vec{B}^2}{(W(\vec{v}^2)+\vec{B}^2)^2} - \vec{Q}^2 = 0. \tag{62}$$

6.2.1. One-dimensional shock-tube problems computed in 1D

We now solve a series of one-dimensional standard shock tube test cases proposed in [3]. For the detailed description of our WENO reconstruction operator in 1D see [26]. The computational domain is $\Omega = [0;1]$ and the initial condition consists of two piecewise constant states on the left and the right of the discontinuity located at $x = 0.5$. The initial states are summarized in Table 8. In all test cases we use $\Gamma = 5/3$ except for the first test case where $\Gamma = 2$ is used, according to [3]. The results of our one-dimensional computations are shown in Figs. 12–16. We use 400 elements in all test cases, except for test case 3 where 800 elements are used, and set the Courant number to CFL = 0.8 in all test cases, except in test case 4, where we use CFL = 0.1. In all test cases, the P_0P_2 scheme is used together with characteristic WENO reconstruction. For a detailed description of the eigenstructure of the RMHD system see [3]. The reference solution is the *exact solution* as published by Giacomazzo and Rezzolla [38]. For all test cases we note a very good agreement between the computations carried out with the new third-order P

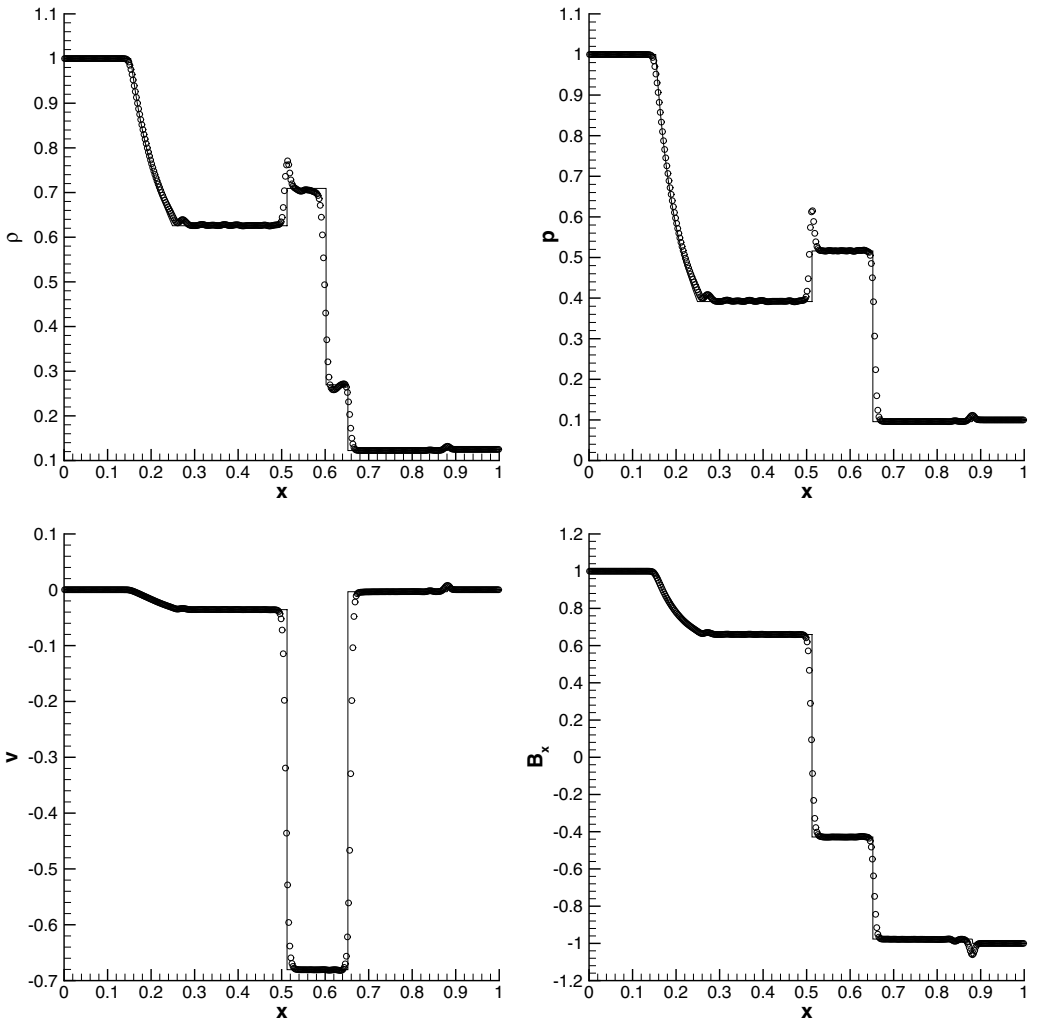

Fig. 12. Numerical results for the relativistic MHD Riemann problem 1 at $t = 0.4$. P_0P_2 scheme on 400 elements (circles) and exact reference solution [38].

solution. Note that the compound wave is present also in our third-order WENO computations as shown for second-order TVD methods by Balsara in [3], but it is not present in the exact reference solution. See [38] for a comment on this topic. In general, our proposed high order scheme remains essentially non-oscillatory. Only small oscillations are visible in most of the test cases. The largest spurious oscillations are produced in test case 2 for the density ρ whereas the other flow quantities remain virtually non-oscillatory. The kink that is visible in the density for the collision test problem number 4 corresponds to the well-known wall heating phenomenon, also present in the computations shown in [3,82] and [46].

6.2.2. One-dimensional shock-tube problem computed in 2D

In this paragraph we show with a simple example that the extension of the one-dimensional P_NP_M method to unstructured multidimensional meshes is straightforward for any hyperbolic system, including even such complicated PDE as the relativistic MHD equations. We solve again test problem number 5 of the previous paragraph, but now on a two-dimensional computational domain $\Omega = [0;1] \times [0;0.05]$ using a 400×20 mesh composed of 17,628 triangles using the P_0P_2 scheme with componentwise WENO reconstruction. The solution of the problem for the density ρ is shown in Fig. 18 together with the triangular mesh. Since the maximum admissible speed in relativistic MHD is the speed of light, we correspondingly choose the divergence cleaning

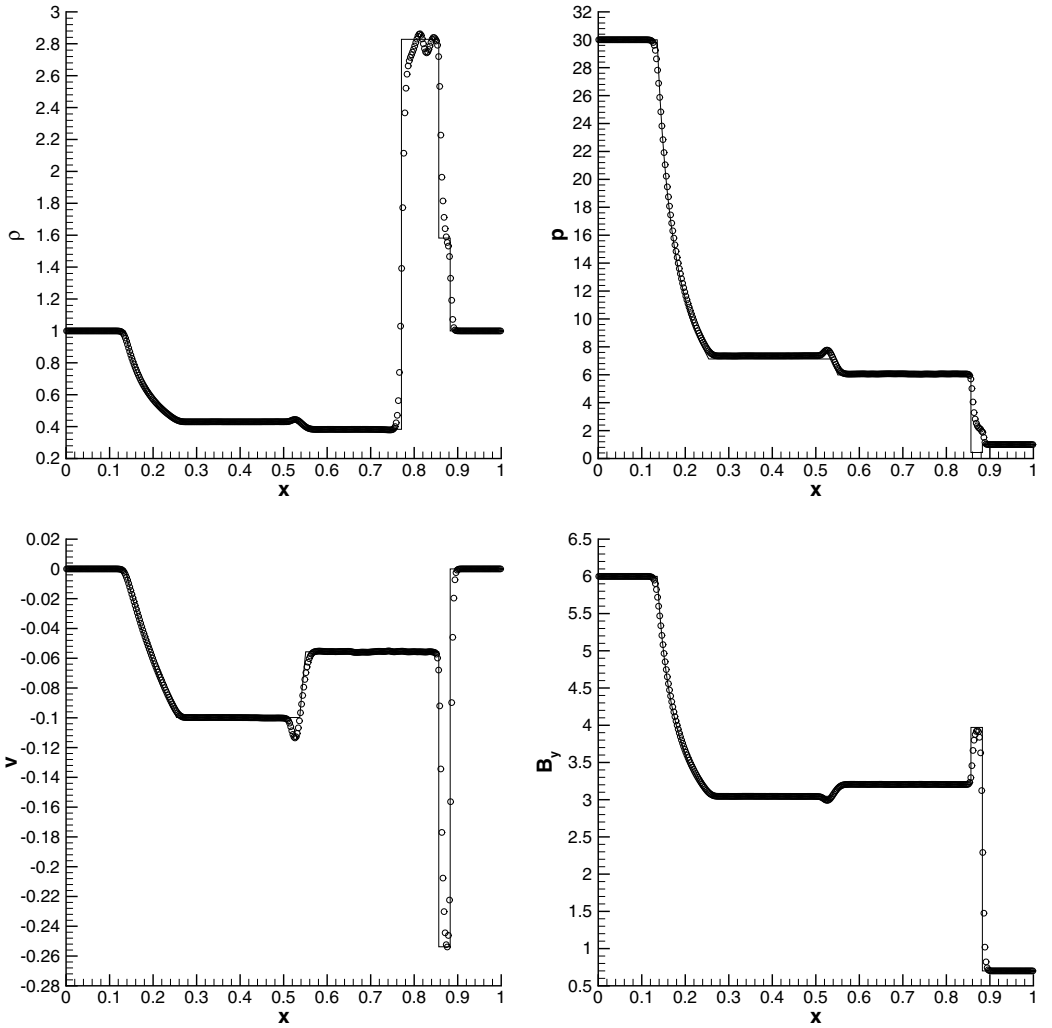

Fig. 13. Numerical results for the relativistic MHD Riemann problem 2 at $t = 0.4$. P_0P_2 scheme on 400 elements (circles) and exact reference solution [38].

speed equal to the speed of light, i.e. $c_h = 1$. A plot of our numerical solution obtained for density ρ is shown in Fig. 18, together with the mesh. To give also a quantitative comparison against the one-dimensional reference solution, a cut through the computational domain is taken parallel to the x-axis at $y = 0.025$. The results obtained with our P_0P_2 scheme and the reference solution are depicted in Fig. 19 and show a very good agreement between our numerical solution and the reference.

6.2.3. Convergence study of some selected P_NP_M schemes for the relativistic MHD equations on triangular meshes in 2D

Since the relativistic MHD equations form a very complicated and very challenging hyperbolic system, we propose to perform again a convergence study of some selected P_NP_M schemes on a very nice time-dependent test case proposed originally in [83]. It consists in a space–time periodic Alfvén wave with large amplitude. The initial condition at $t = 0$ for the primitive variables is chosen to be $\rho = p = 1$, $u = B_x = \Psi = 0$, $B_y = \eta B_0 \cos(kx)$, $B_z = \eta B_0 \sin(kx)$ and $v = -v_A B_y/B_0$, $w = -v_A B_z/B_0$. We use the wavenumber $k = 2\pi$, the 2D computational domain is $\Omega = [0;1] \times [0;0.4]$ with four periodic boundary conditions and $\Gamma = \frac{4}{3}$. With these parameters and $B_0 = \eta = 1$, the speed of the Alfvén wave in positive x-direction is $v_A = 0.38196601125$, see [83] for a

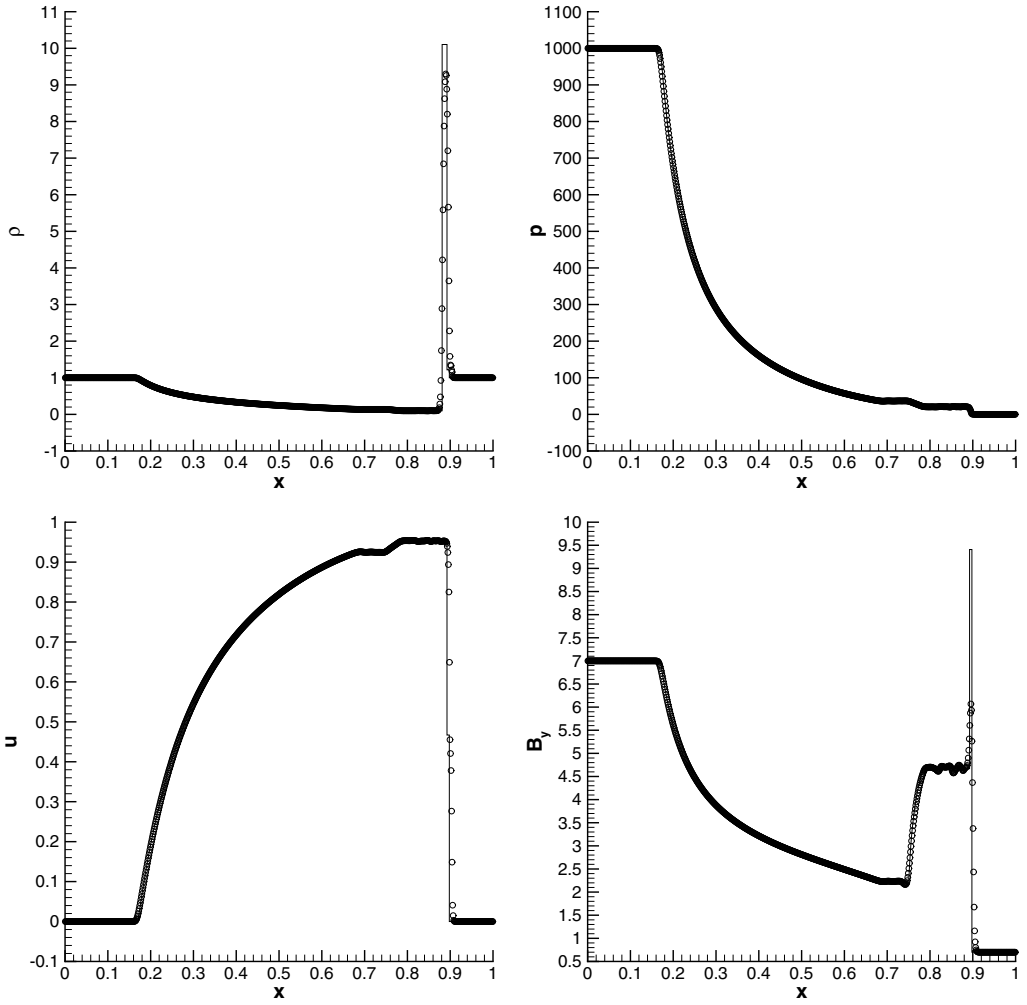

Fig. 14. Numerical results for the relativistic MHD Riemann problem 3 at $t = 0.4$. P_0P_2 scheme on 800 elements (circles) and exact reference solution [38].

closed analytical expression for v_A. Our final computation time is thus $t = 1/v_A = 2.618033988$, which is precisely the travel time that the Alfvén wave needs to complete an entire period. Table 9 shows the errors and measured convergence orders in L^2 norm for the flow variable B_z. The number N_G denotes the number of triangle edges along the x-axis. We underline the very high accuracy that can be achieved at very low computational cost with the P_3P_5 scheme already on the coarsest mesh with $N_G = 4$, see Fig. 17, compared to the third-order finite volume scheme on the finest mesh with $N_G = 128$. In all the computations we use a *constant* Courant number of $0.5/(2N + 1)$, since our method has uniform accuracy in space and time. This could make the new P_NP_M schemes very suitable for highly accurate computations of long-time evolution problems in astrophysics.

6.2.4. RMHD rotor problem

We finally propose to solve two relativistic versions of the MHD rotor problem of Balsara and Spicer [7]. The first is a variation of the relativistic MHD rotor test case already proposed by Del Zanna et al. [82], but with lower rotational speed, in order to show the influence of the initial rotation speed on the produced wave patterns. The second test case is exactly the same as proposed in [82]. We remark that in the second test case, the Lorentz factor is very high ($\gamma \approx 10$) and that high order methods may encounter difficulties with pressure

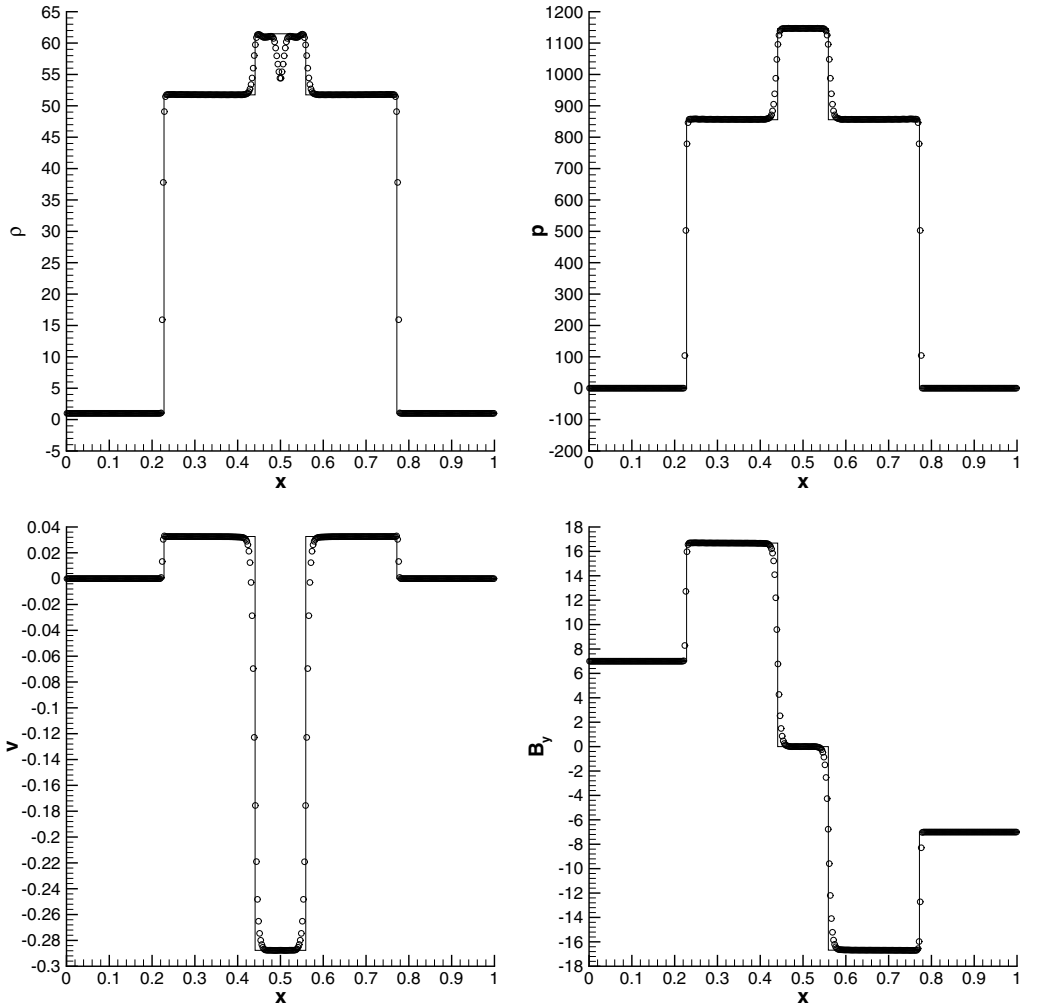

Fig. 15. Numerical results for the relativistic MHD Riemann problem 4 at $t = 0.4$. P_0P_2 scheme on 400 elements (circles) and exact reference solution [38].

positivity. Therefore, a strategy as described in detail in [6] should be applied. In the present paper, we simply reduce the order of accuracy locally to one in those elements where negative pressures are encountered in the time evolution phase.

In contrast to [82], who used a perfectly regular Cartesian mesh on the unit-square, we solve both test cases in Cartesian coordinates on a *circular* computational domain with radius $R = 0.5$ using an *unstructured triangular* mesh with a characteristic mesh spacing of $h = 0.0025$ towards the center and $h = 0.005$ at the outer border of the domain, leading to a total number of 121,196 triangles. The rotor has a radius of $R_i = 0.1$ and is spinning with an angular frequency of $\omega = 8.0$ in the first test case and with $\omega = 9.95$ in the second one, leading to maximal toroidal velocities of $v = 0.8$ and $v = 0.995$, respectively. The density is $\rho = 10$ inside the rotor and $\rho = 1$ in the fluid at rest. The pressure is $p = 1$ and the magnetic field is $\vec{B} = (1, 0, 0)^T$ in the whole domain. We use a P_0P_2 scheme with characteristic WENO reconstruction. No taper is applied to the initial condition, as in [82]. The speed for the hyperbolic divergence cleaning is set constantly to $c_h = 1$ and $\Gamma = 5/3$ is used. Transmissive boundary conditions are applied at the outer boundaries. The whole computational domain together with the results for pressure at output times $t = 0.1$, $t = 0.2$, $t = 0.3$ and $t = 0.4$ is shown in Fig. 20 for the first test case ($\omega = 8.0$) and several flow quantities are shown at $t = 0.4$ in Fig. 21 for the second test case ($\omega = 9.95$). In both cases, we observe the Alfvén waves sent out by the rotor into the medium at rest.

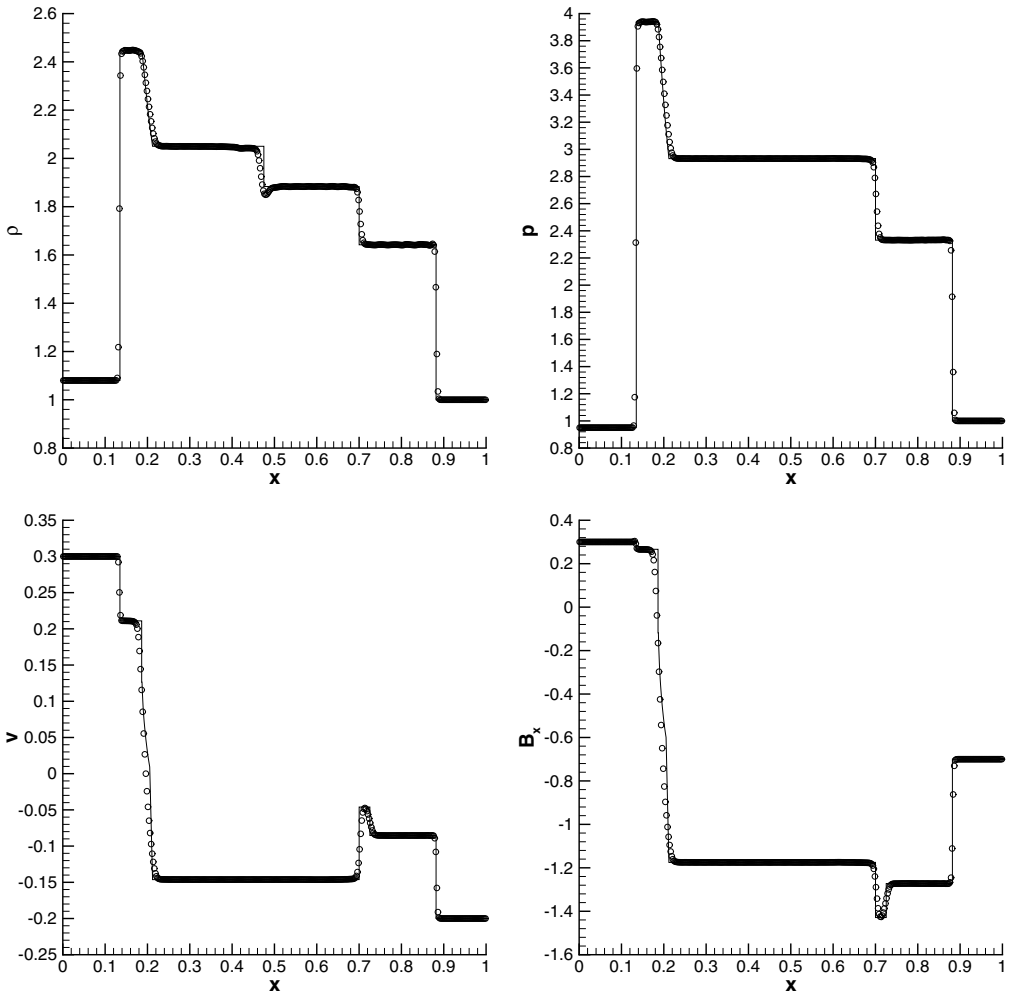

Fig. 16. Numerical results for the relativistic MHD Riemann problem 5 at $t = 0.55$. P_0P_2 scheme on 400 elements (circles) and exact reference solution [38].

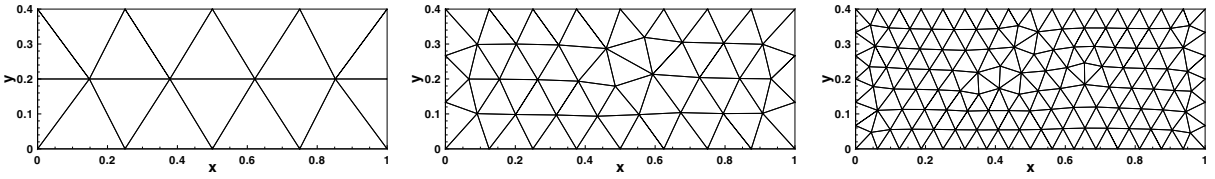

Fig. 17. The coarsest meshes ($N_G = 4, 8, 16$) used for the RMHD convergence test.

For the second test case, we observe a strong roll-up of the shear waves, as reported in [82]. To our knowledge, the computations shown in this article are the first calculations ever done for relativistic MHD using high order WENO finite volume schemes on unstructured triangular meshes.

6.3. Nonlinear elasticity

In this section we consider the equations of nonlinear elasticity (NLE) in Eulerian coordinates as derived by Godunov and Romenski [40–42] and studied numerically in one space dimension by Titarev et al. [69]. We

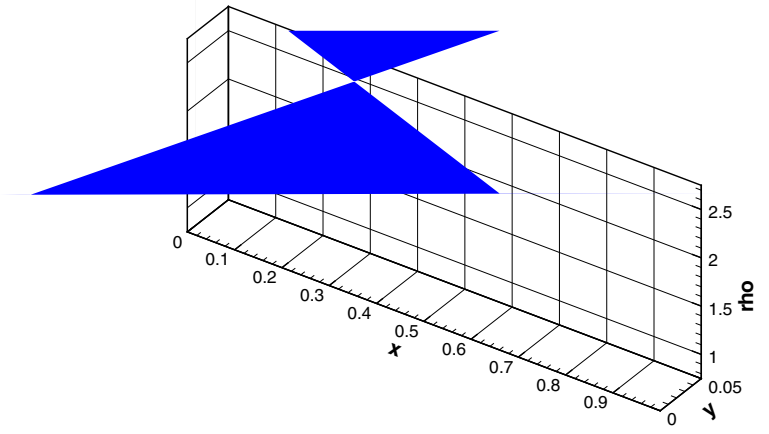
0
0.1
0.2
0.3
0.4
0.5
0.6
0.7
0.8
0.9
x
0
0.05
y
1
1.5
2
2.5
rho

Table 9
Numerical convergence study of some selected $P_N P_M$ schemes for the time-dependent relativistic MHD equations in 2D

N_G	L^2	$\mathcal{O}_{L^2}$	t_{CPU} [s]
P_0P_2			
16	1.68E−02		22.9
32	2.26E−03	2.9	198.3
64	2.77E−04	3.0	2214.2
128	3.44E−05	3.0	16597.6
P_1P_2			
8	1.89E−03		13.5
16	2.12E−04	3.2	76.6
32	2.29E−05	3.2	720.6
64	2.56E−06	3.2	7702.6
P_2P_3			
8	1.40E−04		39.0
16	8.32E−06	4.1	194.6
24	1.48E−06	4.3	1131.5
32	4.79E−07	3.9	2211.0
P_3P_5			
4	3.58E−05		47.8
8	6.71E−07	5.7	178.8
12	7.67E−08	5.3	456.3
16	1.32E−08	6.1	1106.0

mostly follow the notation given in [69], except for the deformation gradient that we call c_{ij} instead of F_{ij} to avoid confusion with the flux tensor of the hyperbolic system in multiple space dimensions. The vector of conservative variables is then $u_p = (\rho, \rho u_i, \rho c_{ij}, \rho E)^{\mathrm{T}}$ and the flux tensor is defined as

$$\vec{F}_p = F_{pk} = \begin{pmatrix} \rho u_k \\ \rho u_i u_k - \sigma_{ik} \\ \rho c_{ij} u_k - \rho c_{kj} u_i \\ u_k \rho E - u_i \sigma_{ik} \end{pmatrix}. \tag{63}$$

Note that according to [69] the equation for density replaces one equation for the deformation gradient, say c_{11}. The total energy is defined as usual as $\rho E = \rho\left(e + \frac{1}{2}\vec{v}^2\right)$. The stress tensor σ_{ij} is a complicated nonlinear function of the deformation gradient c_{ij} and depends on the equation of state (EOS) that is needed to close the system. The EOS defines the internal energy e as a function of the deformation gradient c_{ij} and entropy S as $e = e(c_{ij}, S)$. Then, the following definitions for density ρ, strain tensor g_{ij}, stress tensor σ_{ij} and temperature T hold

$$\rho = \frac{\rho_0}{\det c_{ij}}, \quad g_{ij} = c_{ji}^{-1} c_{jk}^{-1}, \quad \sigma_{ik} = \rho c_{ij} \frac{\partial e}{\partial c_{kj}} = -2\rho g_{ij} \frac{\partial e}{\partial g_{jk}}, \quad T = \frac{\partial e}{\partial S}, \tag{64}$$

where ρ_0 is the constant density in the reference state. In an isotropic medium, the internal energy e is a function of three invariants of the strain tensor g_{ij}:

$$e(I_1, I_2, I_3) = \frac{K_0}{2\alpha^2}\left(I_3^{\alpha/2} - 1\right)^2 + c_V T_0 I_3^{\gamma/2}\left(e^{S/c_V} - 1\right) + \frac{B_0}{2} I_3^{\beta/2}\left(\frac{1}{3} I_1^2 - I_2\right) \tag{65}$$

with the invariants

$$\begin{aligned} &I_1 = \mathrm{tr}(g_{ij}) = g_{11} + g_{22} + g_{33}, \quad I_3 = \det(g_{ij}) = \left(\frac{\rho}{\rho_0}\right)^2, \\ &I_2 = (g_{11}g_{22} - g_{12}g_{21}) + (g_{22}g_{33} - g_{23}g_{32}) + (g_{33}g_{11} - g_{31}g_{13}). \end{aligned} \tag{66}$$

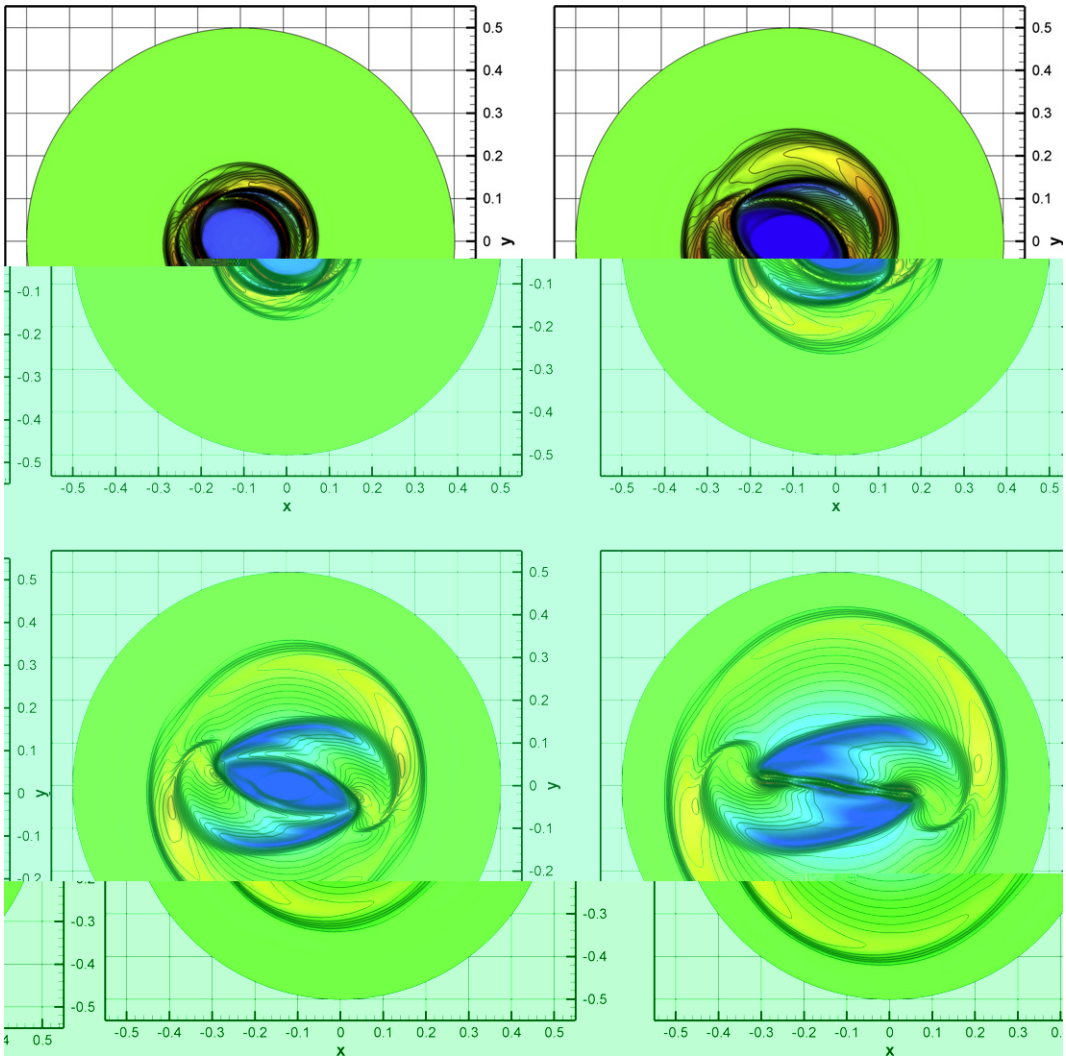

Fig. 20. Results for the pressure p for the first RMHD rotor problem ($\omega = 8.0$) at output times $t = 0.1$, $t = 0.2$, $t = 0.3$ and $t = 0.4$ (top left to bottom right).

In two space dimensions, we always have $g_{33} = 1$. According to [69], K_0 and B_0 are the squared speed of the pressure and the shear wave, respectively, c_V is the heat capacity at constant volume, T_0 is the reference temperature and α, β and γ are constants characterizing the non-linearities in the EOS. Furthermore, there exist constraints in the form of steady PDE for the equations of nonlinear elasticity, similar to the divergence-free condition for the magnetic field in the MHD equations [69]. In nonlinear elasticity they are called the compatibility conditions and are given in terms of the deformation gradient by

$$\frac{\partial \rho c_{1j}}{\partial x} + \frac{\partial \rho c_{2j}}{\partial y} + \frac{\partial \rho c_{3j}}{\partial z} = 0. \tag{67}$$

In our multidimensional computations performed in this section we did not encounter any problems with the compatibility conditions (67), but in long-time evolution problems with high accuracy requirements, a hyperbolic generalized Lagrangian multiplier (GLM) technique as proposed in [23] may become necessary. We first solve two of the one-dimensional shock tube problems proposed in [69] using our P_0P_2 scheme with componentwise WENO reconstruction on the computational domain $\Omega = [0;1] \times [0;0.05]$ on a 200×10 mesh composed of 4420 triangles. The material properties for copper are chosen as in [69], i.e. we use $\rho_0 = 8.9$,

$K_0 = c_0^2 - \frac{4}{3} b_0^2$, $B_0 = b_0^2$, $c_0 = 4.6$, $b_0 = 2.1$, $T_0 = 300$ and $c_v = 0.4 \cdot 10^{-3}$. We use furthermore $\alpha = 1$, $\beta = 3$ and $\gamma = 2$. The shock tube problems are solved on the two-dimensional domain defined above, where periodic boundary conditions are applied in y-direction and transmissive boundaries are imposed in x-direction. The initial condition consists of two piecewise constant states, separated by a discontinuity at $x = 0.5$. The states for both test cases are given in terms of the primitive variables in Table 10. Test case 1 corresponds to the three-wave shock tube problem and test case 2 corresponds to the five-wave shock tube problem described in [69]. The second test case deliberately violates the compatibility condition (67). It consists of two pieces of material that have been subject to different strain conditions and that are afterwards attached to each other. Dr. Titarev kindly provided us with the exact solution of the three-wave shock tube problem and with the numerical reference solution of the five-wave shock tube problem. Our numerical results for the density obtained for both test cases in two space dimensions are shown in Fig. 22, together with the triangular mesh.

Table 10
Initial states left (L) and right (R) for the shock tube problems solved for the equations of nonlinear elasticity and final output times t_e

Case	u	v	c_{11}	c_{12}	c_{21}	c_{22}	S	t_e
1L	0.0	0.0	0.95	0.0	0.0	1.0	0.001	0.06
1R	0.0	0.0	1.0	0.0	0.0	1.0	0.0	
2L	0.0	1.0	0.95	0.0	0.05	1.0	0.001	0.06
2R	0.0	0.0	1.0	0.0	0.0	1.0	0.0	

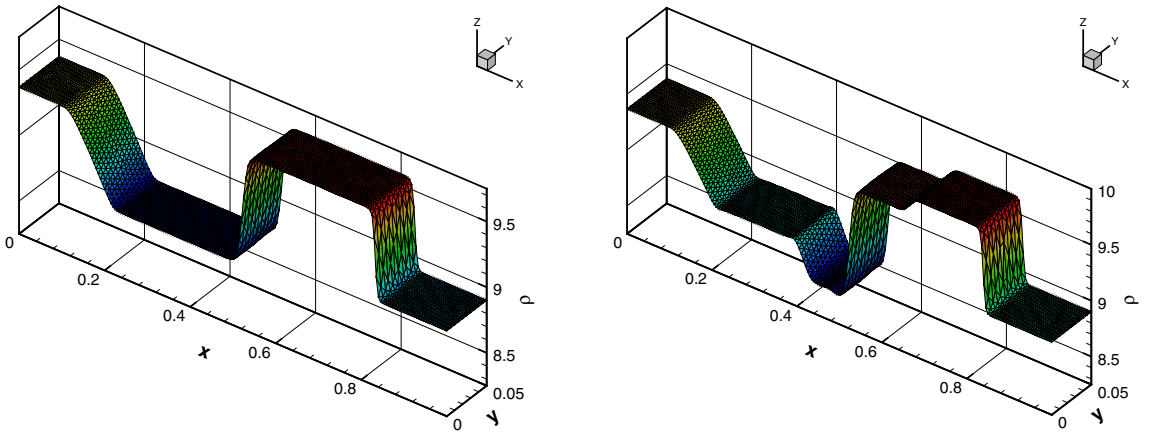

Fig. 22. Numerical results for the two-dimensional version of the three-wave Riemann problem (left) and the five-wave Riemann problem (right) at $t = 0.06$ for the equations of nonlinear elasticity. P_0P_2 scheme on unstructured triangular mesh with componentwise WENO reconstruction.

Finally, we propose a rotor problem for the equations of nonlinear elasticity, similar to the test case shown previously for the two-dimensional ideal MHD equations. The material properties (copper) are identical to the ones used for the shock tube problems. The computational domain is defined by a circle of outer radius $R_o = 0.5$, into which is embedded a rotor of radius $R_i = 0.1$, spinning with a constant angular frequency of $\omega = 10$ so that the tangential velocity is $v_t = \omega R_i = 1$ at $r = R_i$. Density, entropy and deformation gradient are constant $\rho = \rho_0$, $S = 0$ and $c_{ij} = \delta_{ij}$ in the entire computational domain and outside the rotor the velocity is zero. We solve the problem on a triangular mesh with a characteristic mesh size of $h = 0.0025$ at the center of the domain and $h = 0.005$ at the outer boundaries, leading to a total number of 121,196 triangles. This test case may be considered as a highly simplified model for the inner (rotating) and the outer (fixed) part of a bearing which are suddenly attached together via spontaneous welding by friction. The results obtained for the quantities ρu and ρc_{22} are shown in Figs. 24 and 25. We observe fast p-waves travelling into the material at rest and slower shear waves travelling into both the rotor and the stator, thus slowing down the rotor until its final velocity zero is reached.

7. Summary and conclusions

In this article we presented a unified framework for the construction of fully-discrete and very high order accurate quadrature-free one-step finite volume and discontinuous Galerkin schemes on unstructured triangular and tetrahedral meshes in two and three space dimensions. The pure finite volume and DG schemes are only special cases of a more general class of reconstructed P_NP_M schemes, where the data are represented inside each element by piecewise polynomials of degree N and the fluxes and source terms are computed in the final scheme using piecewise polynomials of degree $M \geqslant N$. The new class of intermediate schemes with $M > N$ and $N \neq 0$ produces computationally more efficient algorithms than the traditional finite volume and

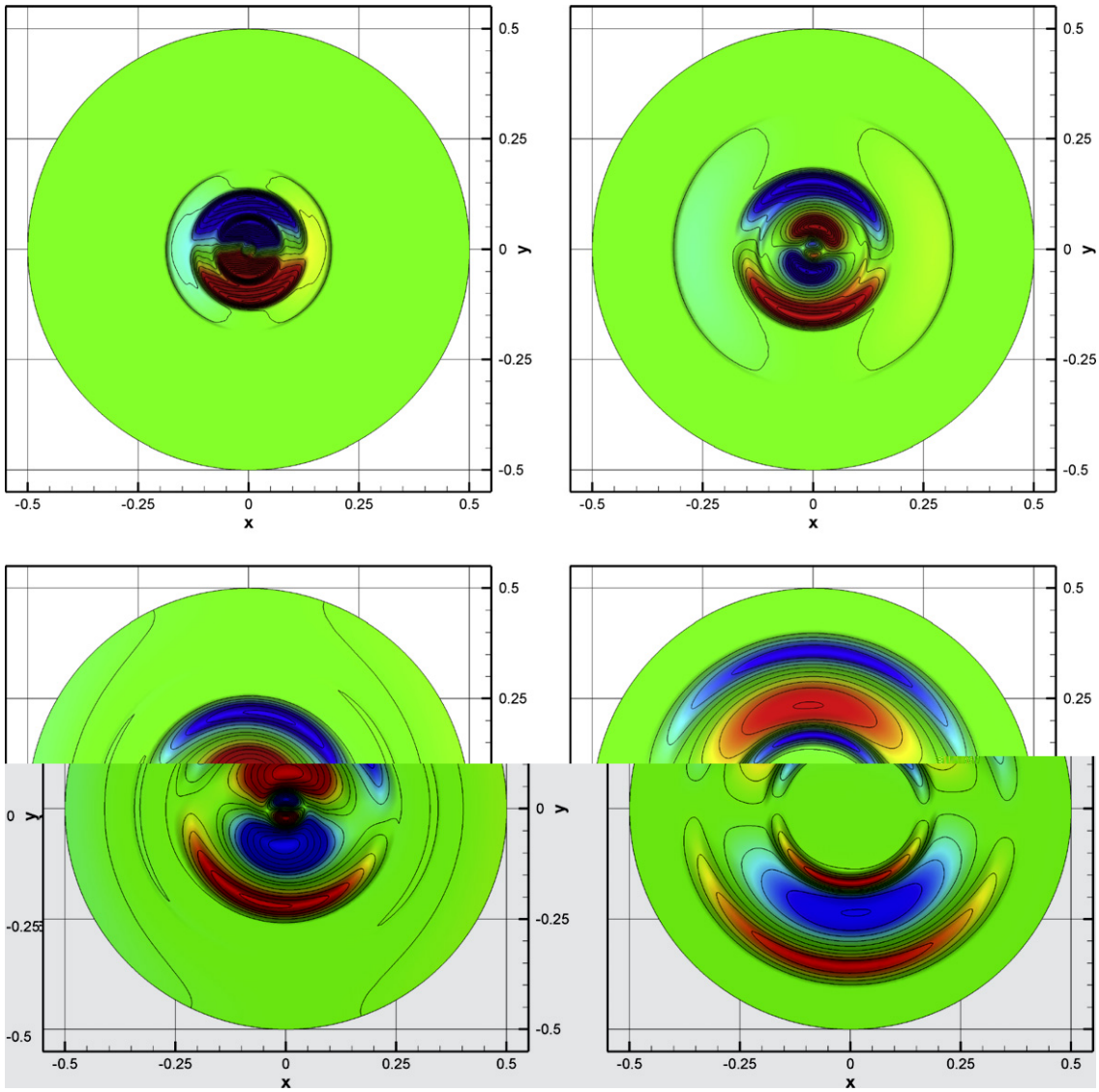

Fig. 24. Results for the quantity ρu for the nonlinear elasticity rotor problem at different output times (top left to bottom right): $t = 0.02$, $t = 0.05$, $t = 0.1$ and $t = 0.2$.

advantages of the new fully-discrete one-step approach compared to TVD Runge–Kutta schemes are (1) its superior MPI efficiency, since no additional MPI communications occur during one time step, (2) its capability to achieve any order of accuracy in time without accuracy barrier, (3) its smaller memory requirements because no intermediate Runge–Kutta stages must be stored and (4) the straight-forward possibility to use all the information produced inside the local space–time continuous Galerkin scheme to construct a globally explicit and fully discrete *quadrature-free* method that does not need time-consuming Gaussian integration in space and that only needs *one* numerical flux computation per element face, independent of the order of accuracy. More details on the MPI parallelization of our method and its MPI efficiency can be found in [27] and [29].

The feasibility of the new approach on unstructured meshes as well as its efficiency and robustness have been demonstrated on a very large set of different complicated hyperbolic equations on unstructured triangular and tetrahedral meshes in two and three space dimensions, ranging from Euler and ideal MHD equations to relativistic MHD and nonlinear elasticity.

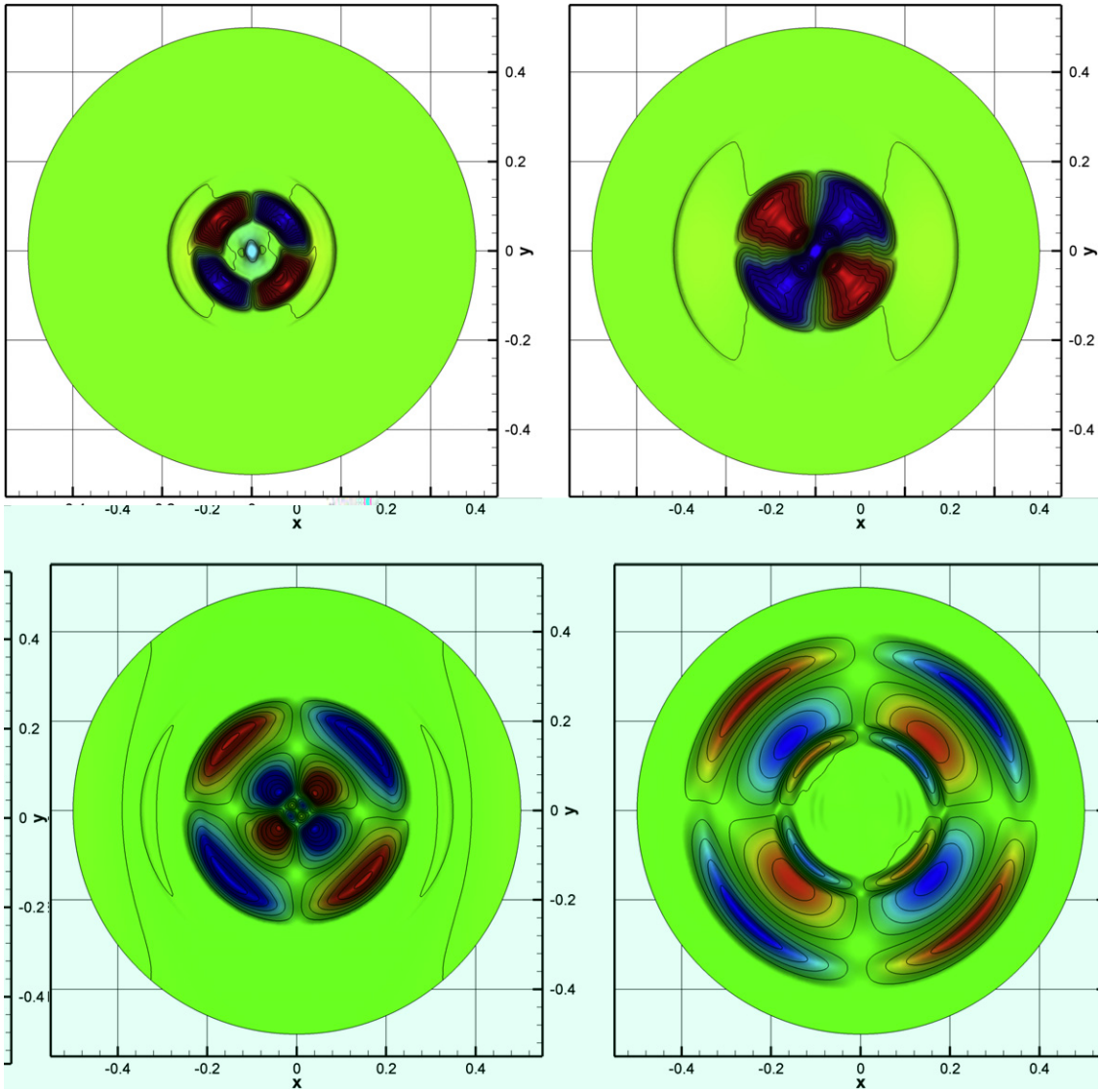

Fig. 25. Results for the quantity ρc_{22} for the nonlinear elasticity rotor problem at different output times (top left to bottom right): $t = 0.02$, $t = 0.05$, $t = 0.1$ and $t = 0.2$.

In our opinion, the proposed unified approach for implementing high order accurate quadrature-free one-step finite volume and discontinuous Galerkin schemes as well as the new class of intermediate schemes may be useful for code developers to include both types of standard discretization methods for hyperbolic PDE in one single software package and let it up to the user to decide whether for his particular application the use of a highly robust finite volume approach or a very accurate DG scheme or even the new class of intermediate methods is the most appropriate.

The most important open problem from an algorithmic point of view, which will be the topic of further research, is the construction of a nonlinear version of our general $P_N P_M$ reconstruction operator. This may lead to a new class of very high order accurate HWENO limiters for DG schemes based on small stencils on unstructured meshes in two and three space dimensions, different from the existing ones.

Another future topic of research will be the generalization of the time-accurate local time stepping approach to $P_N P_M$ schemes, as introduced for ADER-DG schemes on unstructured tetrahedral meshes in

three space dimensions in [30] and as also used in the STE-DG approach for compressible Euler and Navier-Stokes equations in one and two space dimensions presented in [53,37].

Further work will concern the discretization of the compressible Navier–Stokes equations as well as viscous and resistive MHD equations on unstructured triangular and tetrahedral meshes using the new intermediate class of $P_N P_M$ schemes, for which we were able to show in [25] the much more generous stability limits for explicit time-stepping schemes. Work regarding non-conservative hyperbolic systems is currently in progress.

Acknowledgments

The research presented in this paper was financed by the following grants: Michael Dumbser was funded by the *Deutsche Forschungsgemeinschaft* (DFG) in the framework of the *DFG Forschungsstipendium* (DU 1107/1-1). Dinshaw Balsara acknowledges support via NSF Grants R36643-7390002, AST-005569-001, AST-0607731, the NSF-PFC grant PHY02-16783 and the NASA grants HST-AR-10934.01-A and NASA-NNX07AG93G.

The authors would like to thank Olindo Zanotti, Bruno Giacomazzo and Luciano Rezzolla for providing the exact reference solutions for the relativistic MHD test cases. Further help of Dr. Zanotti on the setup of the RMHD convergence test case was highly appreciated. Many thanks also to Vladimir Titarev (Cranfield, UK) for his help concerning the discretization of the equations of nonlinear elasticity and for providing the reference solutions. Finally, we would like to thank the *Leibniz Rechenzentrum* in München, Germany, for providing the necessary supercomputer power needed for the three-dimensional MHD computations shown in this paper.

Appendix A. Example of nodal space–time basis functions and matrices in 1D

In this appendix, we give an example for the space–time basis functions $\theta_l(\xi,\tau)$ as well as the associated temporal and spatial stiffness matrices for a fourth-order scheme ($M = 3$) in one space dimension. The space–time basis functions read as follows:

$$
\begin{aligned}
\theta_1(\xi,\tau) &= 1 - \frac{11}{2}\xi + 9\xi^2 - \frac{9}{2}\xi^3 - \frac{49}{8}\tau + \frac{45}{4}\xi\tau - \frac{27}{4}\xi^2\tau + \frac{189}{16}\tau^2 - \frac{9}{2}\xi\tau^2 - \frac{117}{16}\tau^3\\
\theta_2(\xi,\tau) &= 9\xi - \frac{45}{2}\xi^2 + \frac{27}{2}\xi^3 + \frac{9}{8}\tau - \frac{27}{4}\xi\,\tau + \frac{27}{4}\xi^2\tau - \frac{81}{16}\tau^2 + \frac{81}{16}\tau^3\\
\theta_3(\xi,\tau) &= -\frac{9}{2}\xi + 18\xi^2 - \frac{27}{2}\xi^3 + \frac{9}{8}\tau - \frac{27}{4}\xi\tau + \frac{27}{4}\xi^2\tau - \frac{81}{16}\tau^2 + \frac{81}{16}\tau^3\\
\theta_4(\xi,\tau) &= \xi - \frac{9}{2}\xi^2 + \frac{9}{2}\xi^3 - \frac{13}{8}\tau + \frac{9}{4}\xi\tau - \frac{27}{4}\xi^2\tau + \frac{117}{16}\tau^2 + \frac{9}{2}\xi\tau^2 - \frac{117}{16}\tau^3\\
\theta_5(\xi,\tau) &= 9\tau - 12\xi\tau + 6\xi^2\tau - \frac{45}{2}\tau^2 + 9\xi\tau^2 + \frac{27}{2}\tau^3\\
\theta_6(\xi,\tau) &= -3\tau + 12\xi\tau - 12\xi^2\tau + \frac{27}{2}\tau^2 - \frac{27}{2}\tau^3\\
\theta_7(\xi,\tau) &= 3\tau + 6\xi^2\tau - \frac{27}{2}\tau^2 - 9\xi\tau^2 + \frac{27}{2}\tau^3\\
\theta_8(\xi,\tau) &= -3\tau + \frac{3}{2}\xi\tau + \frac{45}{4}\tau^2 - \frac{9}{2}\xi\tau^2 - \frac{27}{4}\tau^3\\
\theta_9(\xi,\tau) &= -\frac{3}{2}\tau - \frac{3}{2}\xi\tau + \frac{27}{4}\tau^2 + \frac{9}{2}\xi\tau^2 - \frac{27}{4}\tau^3\\
\theta_{10}(\xi,\tau) &= \tau - \frac{9}{2}\tau^2 + \frac{9}{2}\tau^3
\end{aligned}
\tag{A.1}
$$

In order to transform the reconstruction polynomials from the modal space to the nodal space at local time $\tau = 0$ for the local space–time continuous Galerkin scheme, the following transformation via L^2-projection is applied:

$$[\theta_k(\xi,0),\theta_l(\xi,0)]\widehat{\mathcal{U}}_l^0 = [\theta_k(\xi,0),\boldsymbol{\Psi}_m(\xi)]\hat{w}_m \tag{A.2}$$

$$[\theta_k(\xi,0),\theta_l(\xi,0)]^{-1}[\theta_l(\xi,0),\boldsymbol{\Psi}_m(\xi)] = \begin{bmatrix} 1 & -1 & 1 & -1 \\ 1 & -\frac{1}{3} & -\frac{1}{3} & \frac{11}{27} \\ 1 & \frac{1}{3} & -\frac{1}{3} & -\frac{11}{27} \\ 1 & 1 & 1 & 1 \end{bmatrix} \tag{A.3}$$

The temporal stiffness matrix K_{ij}^{τ} is given by

$$K_{ij}^{\tau} = \begin{pmatrix} \frac{67}{640} & -\frac{81}{1280} & -\frac{81}{1280} & \frac{67}{640} & -\frac{13}{80} & \frac{7}{320} & -\frac{21}{80} & \frac{83}{1280} & \frac{211}{1280} & \frac{29}{320} \\ -\frac{267}{1280} & \frac{27}{640} & \frac{27}{640} & -\frac{267}{1280} & \frac{9}{160} & -\frac{9}{320} & \frac{117}{160} & \frac{189}{1280} & -\frac{135}{256} & -\frac{3}{64} \\ -\frac{267}{1280} & \frac{27}{640} & \frac{27}{640} & -\frac{267}{1280} & \frac{117}{160} & -\frac{9}{320} & \frac{9}{160} & -\frac{135}{256} & \frac{189}{1280} & -\frac{3}{64} \\ \frac{67}{640} & -\frac{81}{1280} & -\frac{81}{1280} & \frac{67}{640} & -\frac{21}{80} & \frac{7}{320} & -\frac{13}{80} & \frac{211}{1280} & \frac{83}{1280} & \frac{29}{320} \\ -\frac{5}{16} & -\frac{9}{160} & -\frac{9}{160} & \frac{1}{16} & \frac{3}{5} & \frac{3}{8} & -\frac{3}{20} & -\frac{9}{32} & \frac{3}{32} & -\frac{11}{40} \\ \frac{209}{320} & -\frac{207}{320} & -\frac{207}{320} & \frac{209}{320} & -\frac{51}{40} & \frac{9}{10} & -\frac{51}{40} & \frac{111}{160} & \frac{111}{160} & \frac{1}{4} \\ \frac{1}{16} & -\frac{9}{160} & -\frac{9}{160} & -\frac{5}{16} & -\frac{3}{20} & \frac{3}{8} & \frac{3}{5} & \frac{3}{32} & -\frac{9}{32} & -\frac{11}{40} \\ \frac{93}{1280} & \frac{243}{1280} & \frac{243}{1280} & -\frac{387}{1280} & -\frac{15}{32} & -\frac{111}{160} & \frac{21}{32} & \frac{3}{8} & -\frac{3}{8} & \frac{57}{160} \\ -\frac{387}{1280} & \frac{243}{1280} & \frac{243}{1280} & \frac{93}{1280} & \frac{21}{32} & -\frac{111}{160} & -\frac{15}{32} & -\frac{3}{8} & \frac{3}{8} & \frac{57}{160} \\ -\frac{149}{320} & \frac{27}{64} & \frac{27}{64} & -\frac{149}{320} & \frac{31}{40} & -\frac{5}{4} & \frac{31}{40} & -\frac{57}{160} & -\frac{57}{160} & \frac{1}{2} \end{pmatrix} \tag{A.4}$$

and the spatial stiffness matrix K_{ij}^{ξ} is given by

$$K_{ij}^{\xi} = \begin{pmatrix} \frac{7}{128} & -\frac{69}{320} & \frac{93}{320} & -\frac{83}{640} & \frac{7}{80} & -\frac{1}{5} & \frac{9}{80} & -\frac{67}{640} & \frac{67}{640} & 0 \\ \frac{15}{128} & 0 & -\frac{81}{160} & \frac{249}{640} & -\frac{27}{40} & \frac{27}{20} & -\frac{27}{40} & \frac{63}{640} & -\frac{63}{640} & 0 \\ -\frac{249}{640} & \frac{81}{160} & 0 & -\frac{15}{128} & \frac{27}{40} & -\frac{27}{20} & \frac{27}{40} & \frac{63}{640} & -\frac{63}{640} & 0 \\ \frac{83}{640} & -\frac{93}{320} & \frac{69}{320} & -\frac{7}{128} & -\frac{9}{80} & \frac{1}{5} & -\frac{7}{80} & -\frac{67}{640} & \frac{67}{640} & 0 \\ -\frac{17}{32} & \frac{153}{160} & -\frac{63}{160} & -\frac{1}{32} & \frac{3}{20} & -\frac{1}{2} & \frac{7}{20} & \frac{1}{4} & -\frac{1}{4} & 0 \\ \frac{37}{80} & -\frac{27}{20} & \frac{27}{20} & -\frac{37}{80} & -\frac{1}{4} & 0 & \frac{1}{4} & -\frac{31}{80} & \frac{31}{80} & 0 \\ \frac{1}{32} & \frac{63}{160} & -\frac{153}{160} & \frac{17}{32} & -\frac{7}{20} & \frac{1}{2} & -\frac{3}{20} & \frac{1}{4} & -\frac{1}{4} & 0 \\ \frac{129}{320} & -\frac{27}{64} & -\frac{27}{64} & \frac{141}{320} & -\frac{41}{80} & \frac{5}{4} & -\frac{59}{80} & -\frac{9}{32} & \frac{9}{32} & 0 \\ -\frac{141}{320} & \frac{27}{64} & \frac{27}{64} & -\frac{129}{320} & \frac{59}{80} & -\frac{5}{4} & \frac{41}{80} & -\frac{9}{32} & \frac{9}{32} & 0 \\ -\frac{7}{80} & 0 & 0 & \frac{7}{80} & \frac{1}{4} & 0 & -\frac{1}{4} & -\frac{23}{80} & \frac{23}{80} & 0 \end{pmatrix}. \tag{A.5}$$

References

[1] R. Abgrall, On essentially non-oscillatory schemes on unstructured meshes: analysis and implementation, Journal of Computational Physics 144 (1994) 45–58.

[2] H. Atkins, C.W. Shu, Quadrature-free implementation of the discontinuous Galerkin method for hyperbolic equations, AIAA Journal 36 (1998) 775–782.

[3] D. Balsara, Total variation diminishing scheme for relativistic magneto-hydrodynamics, The Astrophysical Journal Supplement Series 132 (2001) 83–101.

[4] D. Balsara, Second-order accurate schemes for magnetohydrodynamics with divergence-free reconstruction, The Astrophysical Journal Supplement Series 151 (2004) 149–184.

[5] D. Balsara, C. Altmann, C.D. Munz, M. Dumbser, A sub-cell based indicator for troubled zones in RKDG schemes and a novel class of hybrid RKDG + HWENO schemes, Journal of Computational Physics 226 (2007) 586–620.

[6] D. Balsara, D. Spicer, Maintaining pressure positivity in magneto-hydrodynamic simulations, Journal of Computational Physics 148 (1999) 133–148.

[7] D. Balsara, D. Spicerm, A staggered mesh algorithm using high order Godunov fluxes to ensure solenoidal magnetic fields in magnetohydrodynamic simulations, Journal of Computational Physics 149 (1999) 270–292.

[8] T.J. Barth, P.O. Frederickson, Higher order solution of the Euler equations on unstructured grids using quadratic reconstruction, AIAA Paper No. 90-0013, 28th Aerospace Sciences Meeting, January 1990.

[9] M. Ben-Artzi, J. Falcovitz, A second-order Godunov-type scheme for compressible fluid dynamics, Journal of Computational Physics 55 (1984) 1–32.
[10] A. Bourgeade, P. LeFloch, P.A. Raviart, An asymptotic expansion for the solution of the generalized riemann problem. Part II: application to the gas dynamics equations, Annales de l'institut Henri Poincaré (C) Analyse non linéaire 6 (1989) 437–480.
[11] M. Brio, C.C. Wu, An upwind differencing scheme for the equations of ideal magnetohydrodynamics, Journal of Computational Physics 75 (1988) 400–422.
[12] C.C. Castro, E.F. Toro, Solvers for the high-order Riemann problem for hyperbolic balance laws, Journal of Computational Physics 227 (2008) 2481–2513.
[13] B. Cockburn, S. Hou, C.W. Shu, The Runge–Kutta local projection discontinuous Galerkin finite element method for conservation laws IV: the multidimensional case, Mathematics of Computation 54 (1990) 545–581.
[14] B. Cockburn, G.E. Karniadakis, C.W. Shu, Discontinuous Galerkin Methods, Lecture Notes in Computational Science and Engineering, Springer, 2000.
[15] B. Cockburn, S.Y. Lin, C.W. Shu, TVB Runge–Kutta local projection discontinuous Galerkin finite element method for conservation laws III: one dimensional systems, Journal of Computational Physics 84 (1989) 90–113.
[16] B. Cockburn, M. Luskin, C.W. Shu, E. Suli, Enhanced accuracy by post-processing for finite element methods for hyperbolic equations, Mathematics of Computation 72 (2003) 577–606.
[17] B. Cockburn, C.W. Shu, TVB Runge–Kutta local projection discontinuous Galerkin finite element method for conservation laws II: general framework, Mathematics of Computation 52 (1989) 411–435.
[18] B. Cockburn, C.W. Shu, The Runge–Kutta local projection P1-Discontinuous Galerkin finite element method for scalar conservation laws, Mathematical Modelling and Numerical Analysis 25 (1991) 337–361.
[19] B. Cockburn, C.W. Shu, The local discontinuous Galerkin method for time-dependent convection diffusion systems, SIAM Journal on Numerical Analysis 35 (1998) 2440–2463.
[20] B. Cockburn, C.W. Shu, The Runge–Kutta discontinuous Galerkin method for conservation laws V: multidimensional systems, Journal of Computational Physics 141 (1998) 199–224.
[21] B. Cockburn, C.W. Shu, Runge–Kutta discontinuous Galerkin methods for convection-dominated problems, Journal of Scientific Computing 16 (2001) 173–261.
[22] R.B. Dahlburg, J.M. Picone, Evolution of the Orszag–Tang vortex system in a compressible medium. I. initial average subsonic flow, Phys. Fluids B 1 (1989) 2153–2171.
[23] A. Dedner, F. Kemm, D. Kröner, C.-D. Munz, T. Schnitzer, M. Wesenberg, Hyperbolic divergence cleaning for the MHD equations, Journal of Computational Physics 175 (2002) 645–673.
[24] M. Dubiner, Spectral methods on triangles and other domains, Journal of Scientific Computing 6 (1991) 345–390.
[25] M. Dumbser, Arbitrary High Order Schemes for the Solution of Hyperbolic Conservation Laws in Complex Domains, Shaker Verlag, Aachen, 2005.
[26] M. Dumbser, C. Enaux, E.F. Toro, Finite volume schemes of very high order of accuracy for stiff hyperbolic balance laws, Journal of Computational Physics 227 (2008) 3971–4001.
[27] M. Dumbser, M. Käser, Arbitrary high order finite volume schemes for seismic wave propagation on unstructured meshes in 2d and 3d, Geophysical Journal International 171 (2007) 665–694.
[28] M. Dumbser, M. Käser, Arbitrary high order non-oscillatory finite volume schemes on unstructured meshes for linear hyperbolic systems, Journal of Computational Physics 221 (2007) 693–723.
[29] M. Dumbser, M. Käser, V.A. Titarev, E.F. Toro, Quadrature-free non-oscillatory finite volume schemes on unstructured meshes for nonlinear hyperbolic systems, Journal of Computational Physics 226 (2007) 204–243.
[30] M. Dumbser, M. Käser, E.F. Toro, An arbitrary high order discontinuous Galerkin method for elastic waves on unstructured meshes V: local time stepping and p-adaptivity, Geophysical Journal International 171 (2007) 695–717.
[31] M. Dumbser, C.D. Munz, Arbitrary high order Discontinuous Galerkin schemes, in: S. Cordier, T. Goudon, M. Gutnic, E. Sonnendrucker (Eds.), Numerical Methods for Hyperbolic and Kinetic Problems, IRMA Series in Mathematics and Theoretical Physics, EMS Publishing House, 2005, pp. 295–333.
[32] M. Dumbser, C.D. Munz, Building blocks for arbitrary high order discontinuous Galerkin schemes, Journal of Scientific Computing 27 (2006) 215–230.
[33] M.Dumbser, Dumbser, T.Schwartzkopff, Schwartzkopff, C.D.Munz, Munz, Arbitrary High Order Finite Volume Schemes for Linear Wave Propagation, Notes on Numerical Fluid Mechanics and Multidisciplinary Design (NNFM), Springer, 2006, pp. 129–144.
[34] R.W. Dyson, Technique for very high order nonlinear simulation and validation, Technical Report TM-2001-210985, NASA, 2001.
[35] P. Le Floch, P.A. Raviart, An asymptotic expansion for the solution of the generalized riemann problem. Part I: general theory, Annales de l'institut Henri Poincaré (C) Analyse non linéaire 5 (1988) 179–207.
[36] P. Le Floch, L. Tatsien, A global asymptotic expansion for the solution of the generalized riemann problem, Annales de l'institut Henri Poincaré (C) Analyse non linéaire 3 (1991) 321–340.
[37] G. Gassner, F. Loercher, C.D. Munz, A discontinuous Galerkin scheme based on a space–time expansion II. Viscous flow equations in multi dimensions, Journal of Scientific Computing 34 (2008) 260–286.
[38] B. Giacomazzo, L. Rezzolla, The exact solution of the Riemann problem in relativistic magnetohydrodynamics, Journal of Fluid Mechanics 562 (2006) 223–259.
[39] S.K. Godunov, Finite difference methods for the computation of discontinuous solutions of the equations of fluid dynamics, Matematicheskij Sbornik 47 (1959) 271–306.

[40] S.K. Godunov, E.I. Romenski, Nonstationary equations of the nonlinear theory of elasticity in Euler coordinates, Journal of Applied Mechanics and Technical Physics 13 (1972) 868–885.
[41] S.K. Godunov, E.I.Romenski, Romenski, Thermodynamics, conservation laws, and symmetric forms of differential equations in mechanics of continuous media, Computational Fluid Dynamics Review, vol. 95, John Wiley, NY, 1995, pp. 19–31.
[42] S.K. Godunov, E.I. Romenski, Elements of Continuum Mechanics and Conservation Laws, Kluwer Academic/Plenum Publishers, 2003.
[43] S. Gottlieb, C.W. Shu, Total variation diminishing Runge–Kutta schemes, Mathematics of Computation 67 (1988) 73–85.
[44] A. Harten, B. Engquist, S. Osher, S. Chakravarthy, Uniformly high order essentially non-oscillatory schemes, III, Journal of Computational Physics 71 (1987) 231–303.
[45] C. Hirsch, Numerical Computation of Internal and External Flows Vol I: Fundamentals of Numerical Discretisation, Wiley, 1988.
[46] V. Honkkila, P. Janhunen, HLLC solver for ideal relativistic MHD, Journal of Computational Physics 223 (2007) 643–656.
[47] C. Hu, C.W. Shu, Weighted essentially non-oscillatory schemes on triangular meshes, Journal of Computational Physics 150 (1999) 97–127.
[48] G.S. Jiang, C.C. Wu, A high-order WENO finite difference scheme for the equations of ideal magnetohydrodynamics, Journal of Computational Physics 150 (1999) 561–594.
[49] M. Käser, A. Iske, ADER schemes on adaptive triangular meshes for scalar conservation laws, Journal of Computational Physics 205 (2005) 486–508.
[50] V.P. Kolgan, Application of the minimum-derivative principle in the construction of finite-difference schemes for numerical analysis of discontinuous solutions in gas dynamics, Transactions of the Central Aerohydrodynamics Institute 3 (6) (1972) 68–77, (in Russian).
[51] P.D. Lax, B. Wendroff, Systems of conservation laws, Communications in Pure and Applied Mathematics 13 (1960) 217–237.
[52] M.E. Lindelöf, Sur l'application de la méthode des approximations successives aux équations différentielles ordinaires du premier ordre, Comptes rendus hebdomadaires des séances de l'Académie des sciences 114 (1894) 454–457.
[53] F. Loercher, G. Gassner, C.D. Munz, A discontinuous Galerkin scheme based on a space–time expansion. I. Inviscid compressible flow in one space dimension, Journal of Scientific Computing 32 (2007) 175–199.
[54] C. Ollivier-Gooch, M. Van Altena, A high-order-accurate unstructured mesh finite-volume scheme for the advection–diffusion equation, Journal of Computational Physics 181 (2002) 729–752.
[55] S.A. Orszag, C.M. Tang, Small-scale structure of two-dimensional magnetohydrodynamic turbulence, Journal of Fluid Mechanics 90 (1979) 129.
[56] J.M. Picone, R.B. Dahlburg, Evolution of the orszag-tang vortex system in a compressible medium. II. Supersonic flow, Physics of Fluids B 3 (1991) 29–44.
[57] J. Qiu, M. Dumbser, C.W. Shu, The discontinuous Galerkin method with Lax–Wendroff type time discretizations, Computer Methods in Applied Mechanics and Engineering 194 (2005) 4528–4543.
[58] J. Qiu, C.W. Shu, Finite difference WENO schemes with Lax–Wendroff type time discretization, SIAM Journal on Scientific Computing 24 (6) (2003) 2185–2198.
[59] J. Qiu, C.W. Shu, Hermite WENO schemes and their application as limiters for Runge–Kutta discontinuous Galerkin method: one-dimensional case, Journal of Computational Physics 193 (2003) 115–135.
[60] J. Qiu, C.W. Shu, Hermite WENO schemes and their application as limiters for Runge–Kutta discontinuous Galerkin method II: two dimensional case, Computers and Fluids 34 (2005) 642–663.
[61] L. Rezzolla, O. Zanotti, An improved exact riemann solver for relativistic hydrodynamics, Journal of Fluid Mechanics 449 (2001) 395–411.
[62] J.K. Ryan, C.W. Shu, H.L. Atkins, Extension of a post-processing technique for the discontinuous Galerkin method for hyperbolic equations with applications to an aeroacoustic problem, SIAM Journal on Scientific Computing 26 (2005) 821–843.
[63] D. Ryu, T.W. Jones, Numerical magnetohydrodynamics in astrophysics: algorithm and tests for one-dimensional flow, Astrophysical Journal 442 (1995) 228–258.
[64] T. Schwartzkopff, M. Dumbser, C.D. Munz, Fast high order ADER schemes for linear hyperbolic equations, Journal of Computational Physics 197 (2004) 532–539.
[65] C.W. Shu, S. Osher, Efficient implementation of essentially non-oscillatory shock capturing schemes, Journal of Computational Physics 77 (1988) 439–471.
[66] C.W. Shu, S. Osher, Efficient implementation of essentially non-oscillatory shock capturing schemes II, Journal of Computational Physics 83 (1989) 32–78.
[67] A.H. Stroud, Approximate Calculation of Multiple Integrals, Prentice-Hall Inc., Englewood Cliffs, New Jersey, 1971.
[68] A. Taube, M. Dumbser, D. Balsara, C.D. Munz, Arbitrary high order discontinuous Galerkin schemes for the magnetohydrodynamic equations, Journal of Scientific Computing 30 (2007) 441–464.
[69] V.A. Titarev, E.I. Romenski, E.F. Toro, MUSTA-type upwind fluxes for non-linear elasticity, International Journal for Numerical Methods in Engineering 73 (2008) 897–926.
[70] V.A. Titarev, E.F. Toro, ADER: arbitrary high order Godunov approach, Journal of Scientific Computing 17 (1–4) (2002) 609–618.
[71] V.A. Titarev, E.F. Toro, ADER schemes for three-dimensional nonlinear hyperbolic systems, Journal of Computational Physics 204 (2005) 715–736.
[72] E.F. Toro, V.A. Titarev, Derivative Riemann solvers for systems of conservation laws and ADER methods, Journal of Computational Physics 212 (1) (2006) 150–165.

[73] E.F. Toro, R.C. Millington, L.A.M. Nejad, Towards very high order Godunov schemes, in: E.F. Toro (Ed.), Godunov Methods. Theory and Applications, Kluwer/Plenum Academic Publishers, 2001, pp. 905–938.
[74] E.F. Toro, V.A. Titarev, Solution of the generalized Riemann problem for advection–reaction equations, Proceedings of Royal Society of London (2002) 271–281.
[75] J.J.W. van der Vegt, H. van der Ven, Space–time discontinuous Galerkin finite element method with dynamic grid motion for inviscid compressible flows I. General formulation, Journal of Computational Physics 182 (2002) 546–585.
[76] H. van der Ven, J.J.W. van der Vegt, Space–time discontinuous Galerkin finite element method with dynamic grid motion for inviscid compressible flows II. Efficient flux quadrature, Computer Methods in Applied Mechanics and Engineering 191 (2002) 4747–4780.
[77] B. van Leer, Towards the ultimate conservative difference scheme II: monotonicity and conservation combined in a second order scheme, Journal of Computational Physics 14 (1974) 361–370.
[78] B. van Leer, Towards the ultimate conservative difference scheme V: a second order sequel to Godunov's method, Journal of Computational Physics 32 (1979) 101–136.
[79] B. van Leer, On the relationship between the upwind-differencing schemes of Godunov, Engquist-Osher and Roe, SIAM Journal on Scientific and Statistical Computing 5 (1985) 1–20.
[80] B. van Leer, S. Nomura, Discontinuous Galerkin for diffusion, in: Proceedings of 17th AIAA Computational Fluid Dynamics Conference (June 6–9 2005), AIAA-2005-5108.
[81] I.K. Youssef, H.A. El-Arabawy, Picard iteration algorithm combined with Gauss–Seidel technique for initial value problems, Applied Mathematics and Computation 190 (2007) 345–355.
[82] L. Del Zanna, N. Bucciantini, P. Londrillo, An efficient shock-capturing central-type scheme for multidimensional relativistic flows II. Magnetohydrodynamics, Astronomy and Astrophysics 400 (2003) 397–413.
[83] L. Del Zanna, O. Zanotti, N. Bucciantini, P. Londrillo, ECHO: an Eulerian conservative high order scheme for general relativistic magnetohydrodynamics and magnetodynamics, Astronomy and Astrophysics 473 (2007) 11–30.